

Mass flows, turbidity currents and other hydrodynamic consequences of small and moderate earthquakes in the Sea of Marmara

Pierre Henry¹, M Sinan Özeren², Nurettin Yakupoğlu³, Ziyadin Çakır³, Emmanuel de Saint-Léger⁴, Olivier Desprez de Gésincourt⁴, Anders Tengberg⁵, Cristele Chevalier⁶, Christos Papoutsellis¹, Nazmi Postacioğlu⁷, Uğur Dogan⁸, Hayrullah Karabulut⁹, Gülsen Uçarkuş³, M Namık Çağatay³

¹Aix Marseille Univ, CNRS, IRD, INRAE, Coll France, CEREGE, Aix-en-Provence, France, ²Istanbul Technical University, Eurasia Institute of Earth Sciences, Maslak, Istanbul, Turkey, ³Istanbul Technical University, Geological Engineering Dept., Maslak, Istanbul, Turkey, ⁴CNRS, DT INSU, Parc national d'instrumentation océanographique, Plouzané, France, ⁵Aanderaa Data Instruments AS, Bergen, Norway, ⁶Aix Marseille Univ, CNRS, IRD, MIO, Aix-en-Provence, France, ⁷Istanbul Technical University, Physics Dept., Maslak, Istanbul, Turkey, ⁸Yıldız Technical University, Geomatic Engineering Dept., Istanbul, Turkey, ⁹Bogazici University, KOERI, Istanbul, Turkey

Correspondence to: Pierre Henry (henry@cerege.fr)

Abstract. Earthquake-induced submarine slope destabilization is known to cause mass wasting and turbidity currents, but the hydrodynamic processes associated with these events remain poorly understood. Instrumental records are rare, and this notably limits our ability to interpret marine paleoseismological sedimentary records. An instrumented frame comprising a pressure recorder and a Doppler recording current meter deployed at the seafloor in the Sea of Marmara Central Basin recorded the consequences of a $M_w = 5.8$ earthquake occurring Sept 26, 2019 and of a $M_w = 4.7$ foreshock two days before. The smaller event caused sediment resuspension and weak current (< 4 cm/s) in the water column. The larger event triggered a complex response involving a debris flow and turbidity currents with variable velocities and orientations, which may result from multiple slope failures. A long delay

a supprimé: Slow build-up of turbidity currents triggered by a

a supprimé: debris flows

a supprimé: R

a supprimé: scarce

a supprimé: but

a supprimé: no strong

a supprimé: mud

41 of 10 hours is observed between the earthquake and the passing of the strongest
 42 turbidity current. The distance travelled by the sediment particles during the event is
 43 estimated to several kilometres, which could account for a local deposit on a
 44 sediment fan at the outlet of a canyon (where the instrument was located), but
 45 probably not for the covering of the whole basin floor. We show that after a moderate
 46 earthquake, delayed turbidity current initiation may occur, possibly by ignition of a
 47 cloud of resuspended sediment.

a supprimé: Some caution is thus required when tying seismoturbidites with earthquakes of historical importance. However, the horizontal extent of the deposits should remain indicative of the size of the earthquake....

48 1. Introduction

49 Triggering of mass wasting and turbidity currents by earthquakes is a hazard
 50 that can damage seafloor infrastructure (Heezen et al., 1954) and may enhance co-
 51 seismic tsunami generation (Okal and Synolakis, 2001; Synolakis et al., 2002; Hebert
 52 et al., 2005; Ozeren et al., 2010). Earthquake-triggered canyon flushing is also a
 53 primary driver of submarine canyon development and material transfer from
 54 seismically active continental margins to the deep ocean (Mountjoy et al., 2018). It is
 55 often considered that a peak ground acceleration (PGA) of the order of 0.1 g is needed
 56 for an earthquake to trigger a submarine slope failure (Dan et al., 2008; Nakajima and
 57 Kanai, 2000). A peak ground velocity threshold of 16-25 cm/s for turbidity-current-
 58 triggering has been proposed based on observations after 14 November 2016 M_w 7.8
 59 Kaikoura, New Zealand, Earthquake (Howarth et al., 2021). The corresponding peak
 60 ground acceleration cannot be accurately determined because the seismic waveform
 61 in this study was modelled at long periods (> 2 s). Nevertheless, strong motion records
 62 from this earthquake suggest this peak ground velocity threshold does correspond with
 63 a peak ground acceleration of the order of 0.1 g (Bradley et al., 2017). On the other
 64 hand, a global compilation of cable breaks shows that mass flows have been triggered
 65 by individual earthquakes of M_w as low as 3.1 (with esdtimated $PGA \approx 10^{-3} g$) while, on
 66 other margins where sediment input is relatively low and/or earthquakes frequent,
 67 earthquakes >7 M_w failed to trigger cable breaking flows (Pope et al., 2016). In the
 68 Mediterranean region, the threshold is reportedly around $M_w = 5$.

a supprimé: flows

a supprimé: at the seafloor

a supprimé: instability

a mis en forme : Indice

a supprimé: However

a supprimé: ,

a supprimé: exceptionally,

a supprimé: and that,

a mis en forme : Police :Non Italique

a mis en forme : Police :Non Italique

a supprimé: the other hand many $M_w > 7$ have failed to break cables, notably in zones (e.g. Japan Trench) where sediment input is relatively low and earthquakes frequent ...

a mis en forme : Français

a supprimé: successfully

69 In spite of this high regional variability, turbidite deposits in several seismically
 70 active zones have been used as paleoseismological event markers (e.g.: Adams, 1990;
 71 Goldfinger et al., 2003, 2012; McHugh et al., 2014; Ikehara et al., 2016; Polonia et al.,
 72 2016). For instance, Holocene turbidite records in the Sea of Marmara basins display
 73 a recurrence of 200 to 300 years, that roughly corresponds to the recurrence interval

91 of Mw > 6.8 earthquakes (McHugh et al., 2006, 2014; Drab et al., 2012, 2015;
 92 Yakupoğlu et al., 2018). Synchronicity of turbidites over a large area is considered as
 93 the most robust criterion for recognizing sedimentary events caused by large
 94 earthquake ruptures, although this approach has caveats (Talling, 2021; Atwater et al.,
 95 2014). Distinguishing seismoturbidites, caused by earthquakes and related mass
 96 wasting events, and turbidites resulting from other processes (e.g. floods, storms,
 97 sediment loading) from their sedimentological characteristics is particularly challenging
 98 (Talling, 2021; Heerema et al., 2022). Seismoturbidites generally comprise a basal silt-
 99 sand bearing layer under a layer of apparently homogenous mud (named homogenite
 100 or tail) with small or gradual, if any, variations in grain size and chemical composition,
 101 (Polonia et al., 2017; McHugh et al., 2011; Çağatay et al. 2012; Eriş et al., 2012;
 102 Gutierrez-Pastor et al., 2013; Nakajima and Kanai, 2000; Beck et al., 2007). The grain
 103 size break between turbidite and homogenite layers is however not specific to
 104 seismoturbidites and can result from mud settling processes commonly occurring in
 105 turbidity currents (e.g.: Talling et al., 2012). In lakes and closed basins several other
 106 characteristics of turbidite-homogenites, such as the alternation of silt/sand and mud
 107 laminae within a single turbidite unit and presence of bi-directional cross- or flaser-
 108 bedding have been interpreted as indicators of deposition from oscillatory currents
 109 associated with seiches or turbidity current reflection (Beck et al., 2007; Çağatay et al.
 110 2012; McHugh et al., 2011). Indeed, internal tsunami waves and turbidity current
 111 reflection have been recorded after landslides in lakes (Brizuela et al., 2019). However,
 112 seismoturbidites on ocean margins have fairly similar characteristics to those in closed
 113 basins but their layering has been interpreted differently, as a consequence of
 114 confluence (stacked or amalgamated turbidites) or current speed variations (multi-
 115 pulsed turbidites) (Gutierrez-Pastor et al., 2013; Nakajima and Kanai, 2000; Goldfinger
 116 et al., 2003). There is currently a lack of in situ instrumental records that could
 117 substantiate inferred hydrodynamic processes.
 118 Monitoring experiments have generated observations of turbidity currents
 119 flowing in submarine canyons and initiated by meteorological events, seasonal
 120 discharge from rivers and occasionally by landslides (Xu et al., 2004, 2010; Puig et al.,
 121 2004; Palanques et al., 2008; Liu et al., 2012; Khripounoff et al., 2012; Hughes Clarke,
 122 2016; Gwyn Lintern et al., 2016; Azpiroz-Zabala et al., 2017; Paull et al., 2018; Hage
 123 et al., 2019; Normandeau et al., 2020; Heerema et al., 2022). Some turbidity currents
 124 originating from sediment remobilization events are driven by a thick dense basal layer,

a supprimé: This requires d

a supprimé: between

a supprimé: from

a supprimé: those

a supprimé: .

a supprimé:

a supprimé: Seismoturbidites are generally described as turbidite-homogenites where a basal silt-sand bearing layer is overlaid by a layer of apparently homogenous mud with small or gradual, if any, variations in grain size and chemical composition

a supprimé: 3

a déplacé (et inséré) [5]

a supprimé: Holocene seismoturbidite records in the Sea of Marmara basins display a recurrence of 200 to 300 years, that roughly corresponds to the recurrence interval of Mw>7 earthquakes (McHugh et al., 2006, 2014; Drab et al., 2012, 2015; Yakupoğlu et al., 2018; Bulut et al., 2019). In lakes and closed basins several characteristics of deposits following earthquake or landslides, such as ...t

a supprimé: t

a supprimé: sharp boundary

a supprimé: ,

a supprimé:

a supprimé: t

a supprimé: -homogenite

a supprimé: .

a supprimé: S

a supprimé: .

a supprimé:

a supprimé: Monitoring experiments brought records of representative cases of turbidity currents flowing in submarine canyons and initiated by meteorological events and occasionally by landslides

a supprimé: (Azpiroz-Zabala et al., 2017; Khripounoff et al., 2012; ...

a supprimé: . Oscillatory currents resulting from internal waves have been recorded after landslides in lakes (Brizuela et al., 2019).

165 able to displace and bury heavy instruments (Paull et al., 2018). On the other hand,
 166 progressive or pulsed build-up of turbidity current energy is considered typical of
 167 hyperpycnal flows initiated by river floods (Mulder et al., 2003; Khripounoff et al., 2012).
 168 However, the hydrodynamic characteristics of turbidity currents resulting from
 169 landslides and floods may not systematically differ, especially when observations are
 170 done at a distance from the source (Heerema et al., 2022). Most information on
 171 earthquake-triggered events is still indirect based on cable ruptures (e.g.: Gavey et al.,
 172 2017; Pope et al., 2017; Hsu et al., 2008), geomorphological and sedimentological
 173 observations (Mountjoy et al., 2018; Cattaneo et al., 2012; Piper et al., 1999), and
 174 information from displaced instruments (Garfield et al., 1994). In Japan, in situ records
 175 of pressure and temperature were obtained from displaced Ocean Bottom
 176 Seismometers (OBSs) after the Tohoku 2011 M_w 9.1 earthquake (Arai et al., 2013), and
 177 from cabled observatories after the Tokachi-Oki 2003 M_w 8.3 earthquake (Mikada et
 178 al., 2006) and after a moderate (M 5.4) earthquake off Izu Peninsula (Kasaya et al.,
 179 2009). After the large events, strong bottom currents of more than 1 m/s were implied,
 180 generally starting 2-3 hours after the earthquake, with no indication of oscillation or
 181 pulsing. In the off-Izu case a mudflow was observed with a camera 5 minutes after the
 182 earthquake and followed 15 minutes later by a change in current direction and speed.

183 We here present results from an instrumental deployment at the seafloor that
 184 accidentally recorded the consequences of earthquakes that occurred 09/24/2019 and
 185 09/26/2019 in the Sea of Marmara with respective M_w 4.7 and 5.8 (Figure 1A). The
 186 pressure, temperature and current record from this single instrument demonstrate that
 187 both events caused sediment resuspension in turbid clouds, but only the larger event
 188 triggered turbidity currents. However, the instrument suffered a rather complex
 189 sequence of disturbances and a 10 hour delay is observed between the earthquake
 190 and peak current recording. Here, we propose a scenario which could explain the
 191 observations and discuss their implications for the understanding of seismoturbidite
 192 records.

a mis en forme : Couleur de police : Arrière-plan 1

a mis en forme : Couleur de police : Arrière-plan 1, Non Surlignage

a mis en forme : Couleur de police : Arrière-plan 1

a supprimé: On the other hand,

a supprimé: m

a supprimé: combined with

a supprimé:

a supprimé: OBSs

a supprimé:

a supprimé: magnitudes

a mis en forme : Indice

a déplacé vers le haut [5]: Holocene seismoturbidite records in the Sea of Marmara basins display a recurrence of 200 to 300 years, that roughly corresponds to the recurrence interval of $M_w > 7$ earthquakes (McHugh et al., 2006, 2014; Drab et al., 2012, 2015; Yakupoğlu et al., 2018; Bulut et al., 2019).

a supprimé: th

a supprimé: is

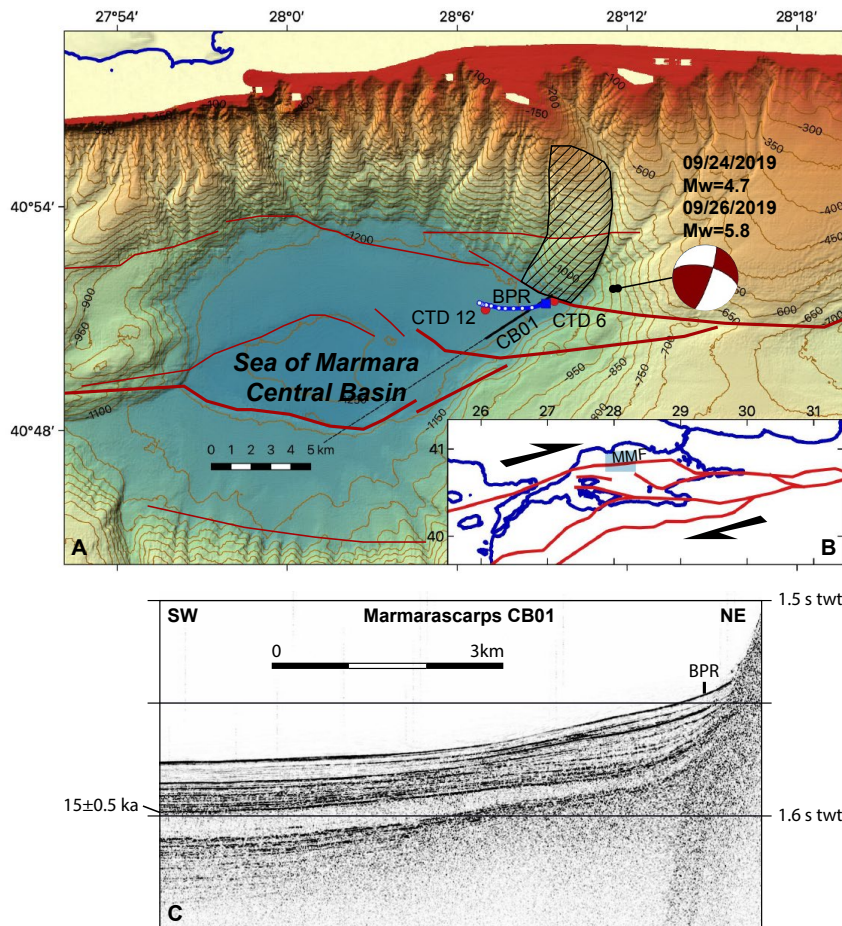
a supprimé: moderate earthquake

a supprimé: s

a supprimé: the recording of

a supprimé: W

a supprimé: here



213
 214 **Figure 1.** Context of instrumental deployment. **(A)** bathymetric map of the Sea of
 215 Marmara Central Basin with simplified fault geometry (in red). The hatched zone is a
 216 suspected mass wasting zone (Zitter et al., 2012). Location of instrumented frame
 217 comprising bottom pressure recorder (BPR) and doppler current meter is indicated by
 218 blue square. The blue banana with white dots represents the calculated trajectory of
 219 a sedimentary particle during the waning phase of the turbidity current. Red dots are
 220 CTD profiles 6 and 12 shown in supplementary material S1. Epicenter location of
 221 earthquakes and the focal mechanism of the main shock are indicated. **(B)** Location
 222 of study area. North Anatolian Fault system is shown in red. MMF is the Main

223 Marmara Fault. (C) Sediment sounder profile from Marmarascarp cruise (Armijo and
224 Malavieille, 2002). Indicative age of reflector from Beck et al. (2007). The instrument
225 (BPR) was deployed on a depositional fan at the base of slope and canyon outlet that
226 differ in seismic character from the reflector sequence in the basin.

a supprimé: the hemipelagite / turbidite-homogenite sequence in the basin

227 2. Context and data collection

228 A series of instrumental deployments was planned to record naturally occurring
229 resonant water column oscillations (seiches) at various locations in the Sea of
230 Marmara with the aim to improve tsunami models (Henry et al., 2021). An instrumented
231 frame was thus deployed at 40.8568° N, 28.1523° E and 1184 m water depth in the
232 Central Basin on May 9, 2019 and recovered six months later (11/19/2019) (Figure 1A).
233 This site is located at the outlet of a complex canyon system with multiple confluence
234 points and tributaries, originating from the edge of the continental shelf (Figure 1).
235 Sediment sounder profiles indicate a depositional fan or lobe is present at this location
236 (Figure 1C). Canyons observed on the relatively steep sedimented slope ($\approx 10^\circ$) of the
237 Sea of Marmara deep basins are presumably fed by mass flows sourced from the
238 canyon heads and walls (Zitter et al., 2012; Çağatay et al., 2015). In addition, the slope
239 west of the canyons immediately north of the deployment site hosts a landslide
240 covering about 24 km² and cores taken at the base of the slope contain a sandy debris
241 flow deposit of 35-40 cm thickness buried 2 m below the seafloor (Zitter et al., 2012).

a supprimé: 6

a supprimé: a

a supprimé: branched canyon system

a supprimé: The short

a supprimé: c

a supprimé: instabilities of the canyon heads and walls

a supprimé: mass wasting feature

242 The Main Marmara Fault (MMF, Figure 1B), is defined as the part of the northern
243 branch of the North Anatolian Fault system crossing the Sea of Marmara (Le Pichon
244 et al., 2001, 2003). A splay of the MMF runs along the base of this slope (Armijo et al.,
245 2002; Grall et al., 2012; Sengor et al., 2014). The 09/24/2019 and 09/26/2019
246 earthquakes occurred under the canyon system and their epicenters are located 5 km
247 ENE of the instrument, less than 500 m apart (Figure 1). The rupture occurred within
248 the crust at 9-13 km depth on a northward dipping fault located north of the principal
249 displacement zone of the Main Marmara Fault. The focal mechanism indicate right-
250 lateral strike-slip with a reverse component (Karabulut et al., 2021). The rupture did
251 not reach the seafloor, nor caused a tsunami. For instance, tidal gauge records
252 obtained at Marmara Ereğlisi do not deviate more than 1 hPa from a fitted tidal model.

a supprimé: beneath

a supprimé: and aftershock distribution

253 The instrumentation on the frame comprises (1) an RBR bottom pressure recorder
254 (BPR) with a Paroscientific 0-2000 m Digiquartz pressure and temperature sensor, (2)
255 a Seaguard recording current meter (RCM) equipped with a Z-pulse 4520 Doppler

a supprimé: g

current sensor operating in the 1.9-2 MHz frequency range and other sensors: temperature, pressure (tide sensor Aanderaa 5217), conductivity (Aanderaa 4319), oxygen (Aanderaa optode 4330) (Figure 2). The RBR pressure and temperature recording interval was set to 5s and that of the Seaguard RCM to one hour for all sensors. The Seaguard instrument was fixed on the upper part of the frame and sensors were 1.5 m above the seafloor. The Z-pulse Doppler current sensor is a single-point current sensor, not an acoustic Doppler profiler (ADCP). It emits four narrow (2°) beams paired in opposite directions along two orthogonal axes, in a plane (parallel to the seafloor if the frame is standing upright), and measures Doppler backscatter in cells extending 0.5-to-2 m from the instrument (Figure 3). The Doppler current sensor was set in burst mode, averaging 150 pings taken every second at the end of each one-hour recording interval and in forward ping mode, so that only data from sensors measuring a positive Doppler shift, upstream currents moving toward the instrument, are used to calculate current speed. The tide sensor is a piezoresistive sensor with a specified accuracy comparable to that of the Digiquartz sensors (4 kPa for a 0-2000 m sensor vs. 2 kPa for a Digiquartz sensor with the same range) and 0.2 hPa (2 mm ocean depth) resolution and comprises a temperature sensor of 0.2°C accuracy and 0.001°C resolution. The tide sensor averages pressure measured at a 2 Hz sampling rate over 300 s at the end of each one-hour time interval. The tide sensor was checked against an atmospheric reference between deployments and found to have a minimal drift, less than 1 hPa. The main purpose of the pressure sensor records was to detect long period variations in water height, related for instance to tides and seiche oscillations but they are also sensitive to pressure variations caused by P-waves. In addition, Digiquartz sensors are intrinsically sensitive to acceleration, but to a small extent, 160 hPa/g for an instrument with 20 MPa range according to the calibration report.

As we will show that the 09/24/2019 earthquake caused the instrumented device to lay on its side for several hours and then straighten up, understanding the setup of the seafloor device and its stability is important (Figure 2B). The frame is made of aluminium and has six rigidly bound flotation spheres of 25 kg buoyancy each. The net weight of the instrumented frame in water is -80 kg. The frame is rigidly attached to a 12-cm-thick 1.5x1.3 m concrete slab, weighing 300 kg in water. The assembly of the heavy slab and buoyant frame is stable in an upright position in the water and on the seafloor. Moreover, it is estimated that a current of 1 m/s would cause a total horizontal

a supprimé: meter

a déplacé vers le bas [2]: The Doppler current meter worked in burst mode, averaging 150 pings taken every second at the end of each one-hour recording interval.

a supprimé: G

a supprimé: and

a supprimé: 4

a supprimé: at

a supprimé: directions

a supprimé: ,

a supprimé: eters

a supprimé: The instrument was set

a déplacé (et inséré) [2]

a supprimé: The Doppler current meter worked in burst mode, averaging 150 pings taken every second at the end of each one-hour recording interval.

a supprimé: t

a déplacé (et inséré) [3]

a supprimé: P

a supprimé: s

a supprimé:

a supprimé: and

a supprimé: also

a supprimé: 6

a supprimé: t

325 drag of 75 kg (≈750 daN) when the device is in upright position, which is insufficient to
326 destabilize it. If a stronger current, or other external forces, cause the assembly to tilt
327 and lay on one side, the moment of the gravity and buoyancy forces should straighten
328 the device back to upright position when these external forces are removed.

329 Measurement of current speed and direction by a tilted instrument is a related issue
330 that we here consider. The orientation and attitude of the Seaguard RCM is measured
331 with a 2-component accelerometer and a magnetic compass and the recorded data
332 include tilt in X and Y direction and the heading of the X axis. Tilt X and Y components
333 are factory calibrated from -35° to +35° with an accuracy of 1.5°. Tests performed in
334 the laboratory (see supplementary material, Figure S1) showed that tilt information
335 remains consistent outside this range, even when the instrument is upside down. Tilt
336 measurements are accurate within 3° up to 60° but saturate at about 80° (Figure S2).
337 Uncertainty on heading also increases with tilt, especially when the instrument is tilted
338 toward the X-direction. However, measured heading remains ±20° of true heading for
339 a tilting of up to 60° (Figure S3). The current measured in the instrument plane is
340 corrected for tilt assuming current is horizontal. As far as this approximation is valid,
341 the current record should in principle remain fairly accurate when the instrument is
342 tilted beyond the normal range of operation (±35° degree) and at least to 60°. However,
343 the compass was not calibrated for an upside-down configuration. If the top of the
344 instrument would happen to be oriented downward, the measured current direction will
345 be unreliable, even though the absolute speed may still be correctly estimated. Another
346 problem may arise if one of the Doppler sensors is facing down into the sediment so
347 that its measurement cell is below the seafloor. If the sensor pointing upward in the
348 opposite direction is recording a negative Doppler shift, this value will be ignored in the
349 forward ping mode. In this case, the measurement retained to calculate current velocity
350 will correspond to noise from the sensor facing toward the seafloor. In all situations, it
351 remains possible to recalculate the sensor readings retained by the calculator from the
352 current velocity and orientation parameters recorded by the instrument by projecting
353 the velocity vector back in the instrument plane, and thus assess the reliability of data.

354 The strength of the backscattered signal can be used as a proxy for turbidity. The
355 Z-pulse emits in the 1.9-2 MHz band corresponding to a wavelength (λ) of 750 μm .
356 Doppler backscatter current meters have maximum sensitivity for particles of diameter
357 $D = \lambda/\pi$ and can detect particles down to diameter $D = 0.08 \lambda$, for which backscatter
358 power is less than 1/10 of peak backscatter power (Guerrero et al., 2011, 2012). The

a déplacé (et inséré) [1]

a supprimé: Seaguard RCM

seaguard RCM should thus be mostly sensitive to the presence in suspension of larger than $63\text{ }\mu\text{m}$. This, however, does not imply that the detected particles are all sand grains in the mineralogical sense, as clay flocs of the same size also cause backscattering.

a supprimé: sand size particles (

a supprimé:)

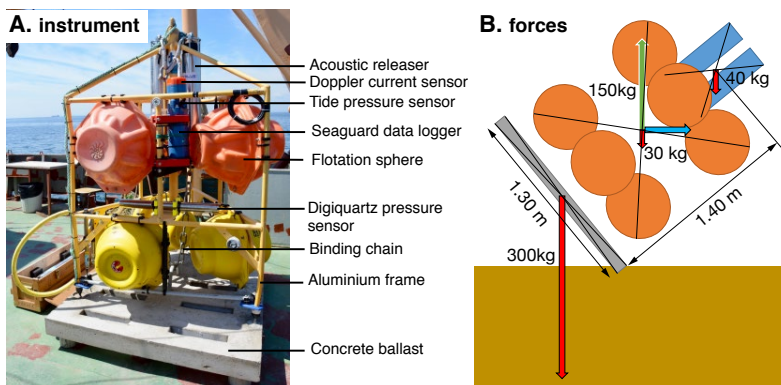


Figure 2. Instrumented frame. (A) photo of the instrumented frame before deployment. (B) Sketch showing forces applied to the elements of the instrumented frame in water. The red arrows represent the weight in water of the cement ballast, of the instrumented frame and of the acoustic release system on top. The green arrow represents the buoyancy of the flotation spheres. The blue arrow represents the current drag, which depends on current speed and instrument tilt.

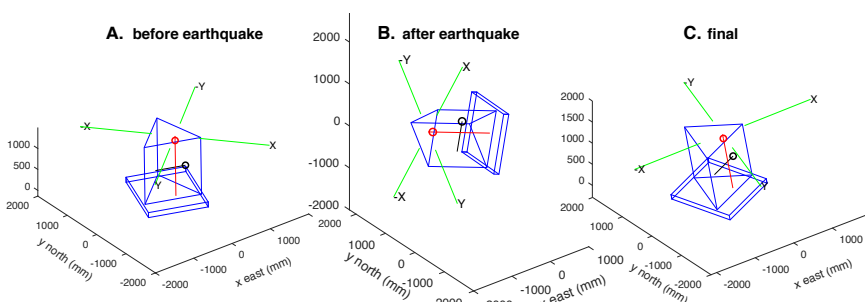


Figure 3. Reconstruction of frame position based on instrument tilt-meter and compass data: (A) before the earthquake; (B) Tilted, between, 25 minutes and 10.5 hours after earthquake; (C) back in nearly upright position 11 hours after earthquake.

380 Position of Digiquartz pressure sensor (black circle), Aanderaa tide sensor (red
381 circle) and Doppler current meter beam cells (green segments)

a supprimé: ¶

383 3. Results

a supprimé: and interpretations

384 3.1. Pressure and tilt records

385 Small earthquakes are detected as pressure spikes, while oscillations are
386 recorded after large earthquakes. The M_w 4.7 09/24/2019 caused a short pressure
387 transient of 25 hPa at 08:00:26 followed by small pressure oscillations of less than 3
388 hPa amplitude decaying over a few minutes. The seismic wave train from the M_w 5.8,
389 09/26/1919 earthquake is recorded by the Digiquartz pressure sensor as oscillations,
390 initiated by a pressure drop of 65 hPa between 10:59:22 and 10:59:26 (Figure 4). For
391 the sampling interval of 5s used in this setup, the recorded signal is aliased, which
392 precludes quantitative interpretation in term of velocity or acceleration. However, the
393 initial pressure drop after the 09/26/1919 earthquake may indicate a negative polarity
394 of the first P-wave arrival at the instrument site, located on an ascending ray-path.

a déplacé vers le haut [3]: Pressure sensors are sensitive to pressure variations caused by P-waves and Digiquartz sensors are also intrinsically sensitive to acceleration, but to a small extent, 160 hPa/g for an instrument with 20 MPa range according to the calibration report. Small earthquakes are detected as

395 Twenty-five minutes after the M_w 5.8 earthquake, a new disturbance of the
396 pressure sensor is observed at 11:23:41. The pressure then progressively increases
397 by 30.9 hPa in 15 seconds between 11:24:46 and 11:25:01 before stabilizing. Over the
398 corresponding one-hour-time-interval between successive records, the Seaguard
399 RCM, initially subvertical (tilt less than 2°), acquires a strong tilt (Figure 3). At 11:57:48,
400 measured tilt is -65° along the X-axis and $+19^\circ$ along the Y-axis, with X-axis in a N161°
401 azimuth and these values remain constant $\pm 2^\circ$ over the next 10 hours, corresponding
402 to an absolute tilt of 68° (Figure 4). The tilting of the instrument causes the Digiquartz
403 and Tide sensors to record different pressure variations because they are located at
404 different positions on the frame (Figure 2). Moreover, the pressure readings by the
405 Digiquartz sensor also depend on its orientation relative to Earth gravity. Pressure at
406 the Tide sensor location increases about 100 kPa, corresponding to a 1 m drop and
407 indicating that the frame was then practically laying on its side. Ten hours later, the
408 device apparently straightens itself in about 5 seconds, between 21:28:29 and
409 21:28:34 as indicated by a rapid pressure variation. After that, the recorded tilt
410 parameters are moderate and stabilize at -11.5° for the X-axis and 5.3° for the Y-axis,
411 with X-axis in a N105.3° azimuth.

a supprimé: ,

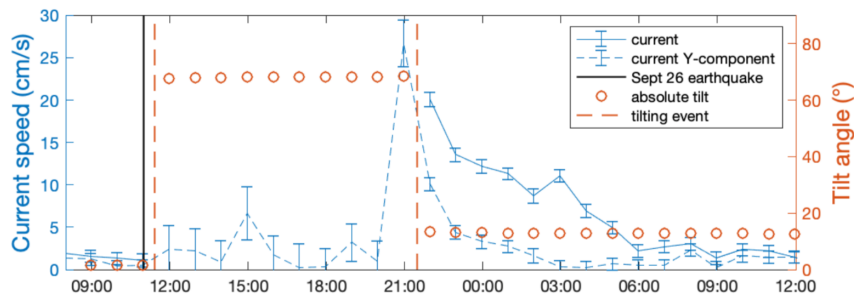
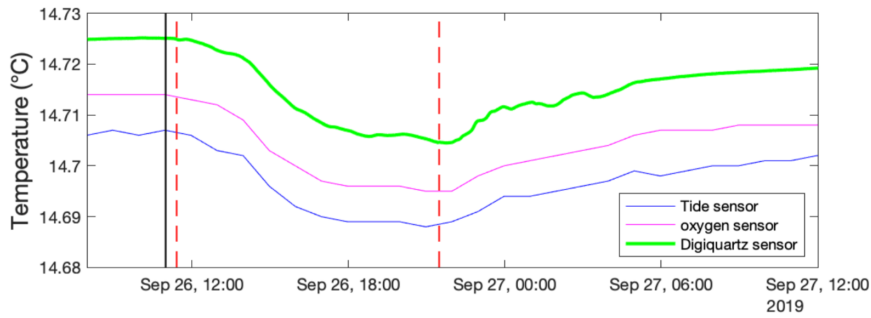
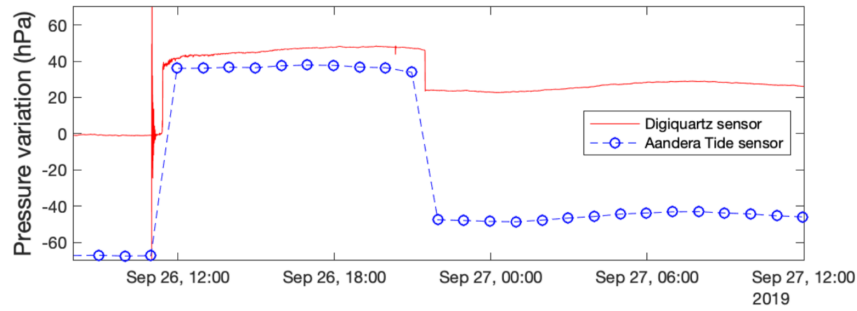
421 Baseline changes before and after the earthquake correspond to an increase of
422 23 hPa for the Digiquartz sensor and 20 hPa for the Tide sensor. These concur that
423 the instrumented frame was about 20 cm deeper after returning to upright position.
424 Considering that the slope at the location of the instrument is about 1%, this may
425 correspond to a 20 m lateral downslope displacement. However, in the absence of
426 other information, it is not known whether the pressure baseline change is a
427 consequence of instrument lateral displacement or burial in place.

428 The M_w 4.7 earthquake caused minor disturbances of the attitude of the
429 instrument, with variations of tilt and heading of less than 0.5° . A M_w 3.6 foreshock of
430 the M_w 5.8 occurring 26/09/2019 at 7:32 also caused minor disturbances. These
431 indicate that the seafloor was sensitive to ground shaking caused by these small
432 earthquakes. However, this did not cause the device to sink into the sediment.
433 Changes of the pressure baseline of the digiquartz sensor between before and after
434 these earthquakes are difficult to resolve, and correspond to less than 5 mm vertical
435 displacement for the first event and less than 2 mm for the second one.

a supprimé: ,

a supprimé: h

439



440

441 **Figure 4.** Time series around the time of occurrence of a M_w 5.8 earthquake; (top)
 442 pressure variations recorded by two instruments on the instrumented frame; (middle)
 443 temperature records from Digiquartz, Tide and oxygen sensors; (bottom) current and
 444 tilt data recorded by Seaguard RCM. Between the tilting events only one component
 445 of the doppler current meter functioned reliably (Y-component oriented N200) and is
 446 here reported.

a supprimé:

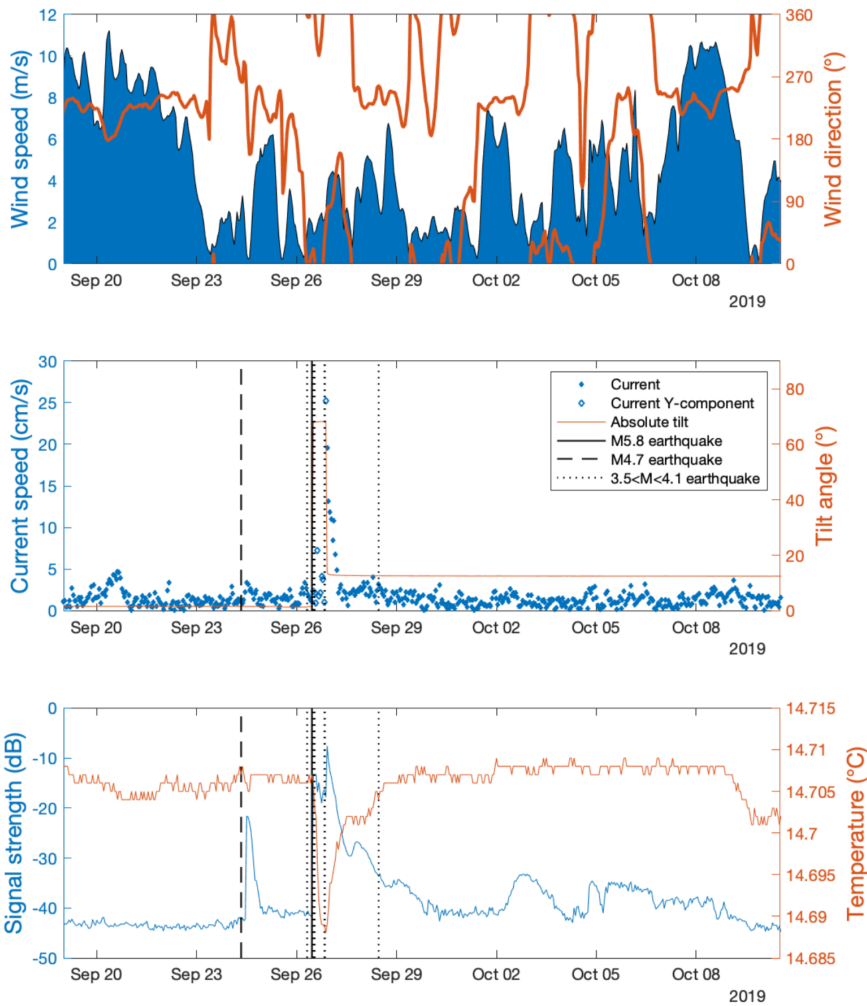


Figure 5. Time series acquired with Seaguard RCM during the September 2019 seismicity cluster and ERA5 reanalysed meteorological data (Hersbach et al., 2018); (top) ERA5 wind data, (middle) current speed and tilt; (bottom) backscatter signal strength and temperature.

a supprimé:

a supprimé: top

3.2. Current records

The M_w 4.7 09/24/2019 earthquake was followed by a small increase of current strength peaking at 3.4 cm/s at noon, four hours after the earthquake (Figure 5). Comparable events in term of duration and strength occurred spontaneously 09/20/2019 (with currents up to 4.7 cm/s) and 09/26/2019 (with currents up to 3.3 cm/s) just before the M_w 5.8 earthquake. During all three events the dominant current was from the east, thus coming from the direction of the canyon, but there is an important difference between the event that occurred after the M_w 4.7 earthquake and the two others. During that event a change in current direction occurred from eastward to westward between 10:57 and 11:57 while the current strength increased from 2.2 cm/s to its peak value of 3.4 cm/s (Figure 6). During the other events, build-up was more progressive and did not involve a change in direction. A drift plot, calculated by summing velocity vectors over time, reproduces the motion of a particle assuming a uniform velocity field (Figure 6). The total drift occurring in the 8 hours following the current inversion is about 500 m. Current direction varies from westward to northward during this time interval.

a supprimé: and possible causes of tilting

a supprimé: 4

a mis en forme : Non Surlignage

a mis en forme : Indice

a supprimé: main

a supprimé: is about 500 m and

a supprimé: S

a supprimé: W

a supprimé: N

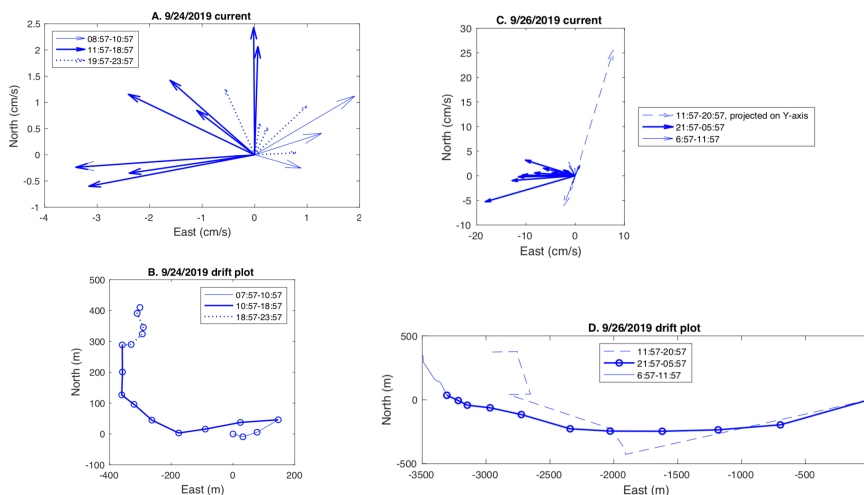


Figure 6. Current recorded after M_w 4.7 and M_w 5.8 earthquakes: (A) Current velocity arrows recorded every hour between 08:57 and 23:57 on 09/24/2019; (B) drift plot over the same time interval, the change of current direction and strength between

486 10:57 and 11:57 coincides with increasing backscatter strength (see figure 4),
 487 indicative of increased turbidity; (C) Current velocity arrows recorded every hour
 488 between 12:00 09/26/2019 and 06:00 09/27/2019. Dashed arrows show
 489 measurements acquired in the Y direction when the instrument was strongly tilted
 490 (position B in Figure 3), plain arrows when it was back in upright position (C in Figure
 491 3); (D) drift plot over the same time interval, the dashed part corresponds to the
 492 strongly tilted position.

493
 494 After the M_w 5.8 09/26/1919 earthquake, during the 10 hour period when the
 495 instrument remained strongly tilted, the instrument recorded currents varying both in
 496 speed and orientation, but some precautions are needed when interpreting these data.
 497 The current component measured by transducers along the Y-axis of the instrument,
 498 oriented N200°, probably remained accurate as the tilt along this axis is less than 20°
 499 and the measurement cell remained above the bottom (Figure 2B). On the other hand,
 500 the X-component may not be reliable as one of the sensors (n°1) is oriented 65°
 501 upward in the N160° direction, and the oposite sensor (n°3) is dipping 65° downward
 502 in the opposite (N340°) direction. Consequently, measurement cell n°3 lies within the
 503 sediment and thus may only record noise. Moreover, because the Doppler current
 504 sensor (DCS) is set in forward pinging mode, current speed is calculated with data
 505 from sensors measuring positive doppler shifts only. This implies that if the current
 506 component toward N160° is positive, sensor n°1 will measure a negative shift and will
 507 not be recorded. During the time interval considered here, the mesured current
 508 component in the X-direction (toward N160) is positive, which indicates that data from
 509 sensor n°3 was used (Figure 7), and that is probably noise. It follows that the current
 510 component along the Y-direction is the only one reliable. The horizontal current
 511 measured along the Y-axis changed sign several times during this time interval, and
 512 reached peak values of 6.3 cm/s toward N200 at 14:57:46, about four hours after the
 513 earthquake, and of 25 cm/s in the oposite direction at 20:57:46, the last measurement
 514 before the instrument straightenned up. Other measurements on both axes remain
 515 below 5 cm/s, but the absolute velocity may have been higher because this
 516 measurement was only performed in one direction. Yet, these observartions suggest
 517 that the stronger current (25 cm/s) recorded 30 minutes before the instrument
 518 straightenned up played a role in this event. Once the device got back in an upright
 519 position, it recorded a current consistently flowing westward and progressively

a supprimé: ¶

a mis en forme : Gauche, Retrait : Première ligne : 0 cm

a supprimé: r

a supprimé: s

a supprimé: here

a supprimé: 4

a supprimé:

a supprimé:

decreasing from 20 cm/s to background level (2 cm/s) in nine hours (Figure 4). During this waning phase, the current drift is about 3.5 km in a westward direction (Figure 6). The drift estimated during the first 10 hours after the earthquake, while the instrument was strongly tilted, is in the opposite direction but may not be reliable.

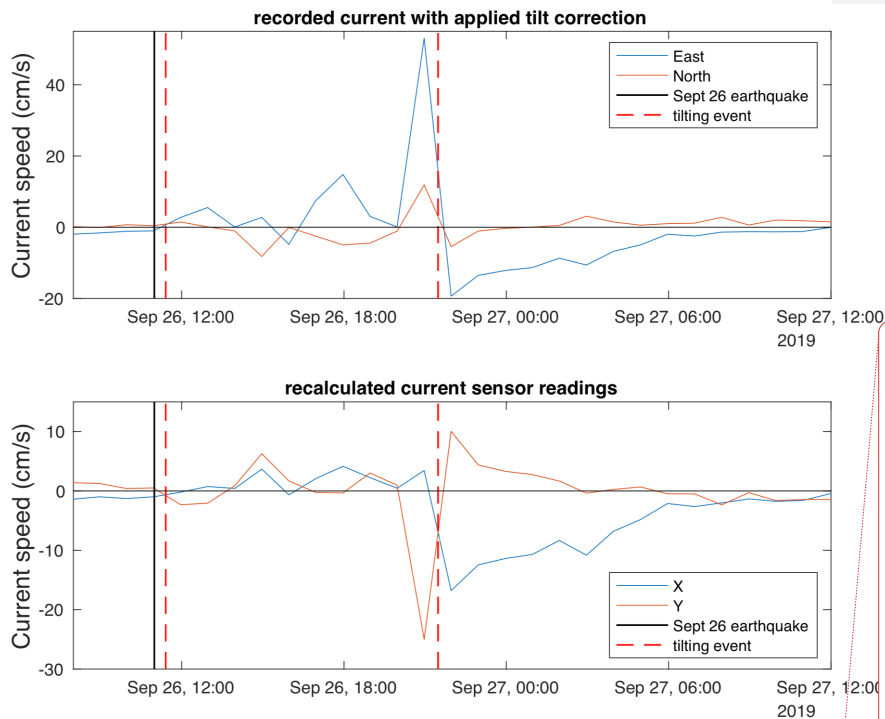


Figure 7. Current record acquired around the time of occurrence of a M_w 5.8 earthquake. A. Instrumental record, automatically corrected for tilt and heading. B. recalculated readings in the X and Y axis of the Doppler sensor (see text for interpretation).

3.3. Acoustic backscatter signal.

The background backscatter amplitude level is -43 ± 1 dB before the earthquakes.

Three to four hours after the M_w 4.7 09/24/2019 earthquake, backscatter increases sharply to -22 dB between 11:00 and 12:00, and then decays to -41 dB over 12 hours. The increase of backscatter coincides with a change of current direction and speed,

a supprimé: 9

a supprimé: ¶

The current speed in the first 2 hours after the main earthquake apparently remained low, at most 5-6 cm/s. It is thus unlikely that the tilt of the device was caused by strong currents. Some short burst of current may have been missed because of the 1 hour sampling interval, but this would not explain why the frame then remained stable in a tilted position for several hours. Local liquefaction of the sediment beneath the device is also an unlikely cause because the tilting of the instrument occurred 25 minutes after the earthquake. A mud flow originating from the basin slopes thus appears as a more likely cause. This hypothesis would also account for the presence of sandy mud caked on the device in various places: on the frame feet, on the acoustic releasers, on the optode connector and also inside the plastic protection of a flotation sphere, from which bindings were broken and had to be repaired. On the other hand, the current speed in the 20-50 cm/s range recorded before, as well as after, the time when the device straightened up is strong enough to cause erosion of mud or sand deposits. It may thus be hypothesized that erosion freed the device from the mud cover. The flotation spheres on the frame and the concrete ballast at its base exert a moment that should keep the assembly stable in an upright position unless the frame is loaded with sediment. ¶

a supprimé: record

a déplacé vers le haut [1]: The strength of the backscattered signal can be used as a proxy for turbidity. The Seaguard RCM emits in the 1.9-2 MHz band corresponding to a wavelength (λ) of 750 μm . Doppler backscatter current meters have maximum sensitivity for particles of diameter $D = \lambda/\pi$ and can detect particles down to diameter $D = 0.08 \lambda$, for which backscatter power is less than 1/10 of peak backscatter power (Guerrero et al., 2011, 2012). The seaguard RCM should thus be mostly sensitive to the presence in suspension of sand size particles (larger than 63 μm).

a supprimé: in

584 indicating that the turbid cloud was brought to the instrument site by the current.
 585 However, the current speed of less than 4 cm/s may have been insufficient to put the
 586 particles in suspension. There is no increase of backscatter on Sept 20 when stronger
 587 currents coming from the same direction, but not related with an earthquake, were
 588 recorded.

589 Backscatter strength remains -41 ± 1 dB for the 1.5 day interval before the M_w 5.8
 590 09/26/1919 and increases to the -20 dB to -13 dB range after the earthquake (Figure
 591 5). This implies sand sized particles or flocs were put in suspension soon after the
 592 earthquake although the local current speed remained relatively low (about 5 cm/s at
 593 most). After the device went back to near vertical position, signal strength reaches a
 594 maximum of -7.6 dB, which correspond to an amplitude ratio of 42 and an intensity
 595 ratio of 1800 compared to base level. Similar signal strength levels are typically
 596 reached with the Z-Pulse sensor in highly turbid water such as in estuaries. During
 597 deep sea deployments signal strength range more typically between -60 and -40 dB.
 598 After reaching peak value, backscattered signal strength progressively decays over 3
 599 days to stabilise at about -40 dB (Figure 5). Several turbid events, with signal strength
 600 about -35 dB are observed in October and associated with small increases in current
 601 velocity (up to 3-4 cm/s). It is unclear whether these passing clouds are residual
 602 turbidity from the earthquake. After October 9, backscatter eventually returns to
 603 background level while temperature decreases by 0.007 °C over a few hours,
 604 indicating replacement of the water mass around the instrument.

606 3.4. Temperature record

607 The Sea of Marmara is stratified, with a low salinity (20-22‰) 20-30 m surface
 608 layer that displays strong seasonal temperature variability (5-10°C in winter, 20-25°C
 609 in summer) overlaying a high salinity (about 38‰) body of seawater at 14-15°C derived
 610 from the Aegean Sea (Beşiktepe et al., 1994). Within the high salinity body, the
 611 conservative temperature (McDougall et al., 2013) calculated with the Gibbs Seawater
 612 oceanographic toolbox of TEOS-10 (McDougall and Barker, 2011) generally
 613 decreases with depth. This implies that the adiabatic temperature rise in a turbidity
 614 current, flowing downward, should cause a small temperature increase at the location
 615 of the instrument. However, the deployment site is prone to seasonal cascading within
 616 the deep water body, so that the initial temperature structure may have been disturbed.

a supprimé: s

a supprimé:

a supprimé: , which

a supprimé: sediment

a supprimé: as

a supprimé: 3 days

a supprimé: is

a supprimé: potential

a supprimé:

a supprimé: , which would in principle

a supprimé: y

a supprimé: a

a supprimé: should

a supprimé:

a supprimé: increase

Examples of CTD profiles recorded in June 2007 (Henry et al., 2007) are shown in Figure 8 and indicate the presence of a slightly warmer water body on the seafloor, only present in the basin along the base of the slope. No CTD profile is available in Sept 2019, but variations in temperature and oxygen concentration associated with mild currents (<5 cm/s) were recorded by the instrument in May-July 2019, and again on Sept 20. It is therefore likely that the temperature at the location of the instrument was slightly higher, by 0.01 to 0.02°C, than at the same depth in the central part of the basin.

Temperature variations associated with the M_w 4.7 09/24/2019 earthquakes are very small, less than $\pm 0.002^\circ\text{C}$, which confirms that water movements during this event were local. After the M_w 5.8 09/26/2019 earthquake, the recorded temperature decreases progressively by about 0.015°C to reach its minimum value when the strongest current is recorded, around the time when the instrument straightens itself (Figure 5). After that, temperature progressively increases back to reach nearly the same value as before the event. The small variation in temperature indicates that the turbid water originates from within the deep-water body. One remarkable observation is that temperature only starts decreasing very slowly after the tilting of the instrument. Temperature decreases at a higher rate after 14h, which is also when the tilted instrument start measuring significant currents.

The slight temperature decrease observed after the earthquake can result from the mixing of the warmer bottom water body originally present around the instrument, with the bulk of the deep-water layer in the Central Basin. Moreover, the observation of a temperature drop precludes that the turbid water originates from depths less than 600 m, as water present between 600 m and the halocline is at a higher conservative temperature than the deeper water throughout the year (see Beşiktepe et al., 1994, and figure 8). Moreover, an inflow of water from closer to the surface should result in an increase in the O_2 concentration in the bottom water, but none is observed in the data.

a supprimé: .

a supprimé: did not travel far during this event

a supprimé: ,

a supprimé: , after the first hydrologic disturbance and tilting of the instrument, until the recorded current reaches its maximum value

a supprimé: T

a supprimé: then

a supprimé: recorded

a supprimé: a

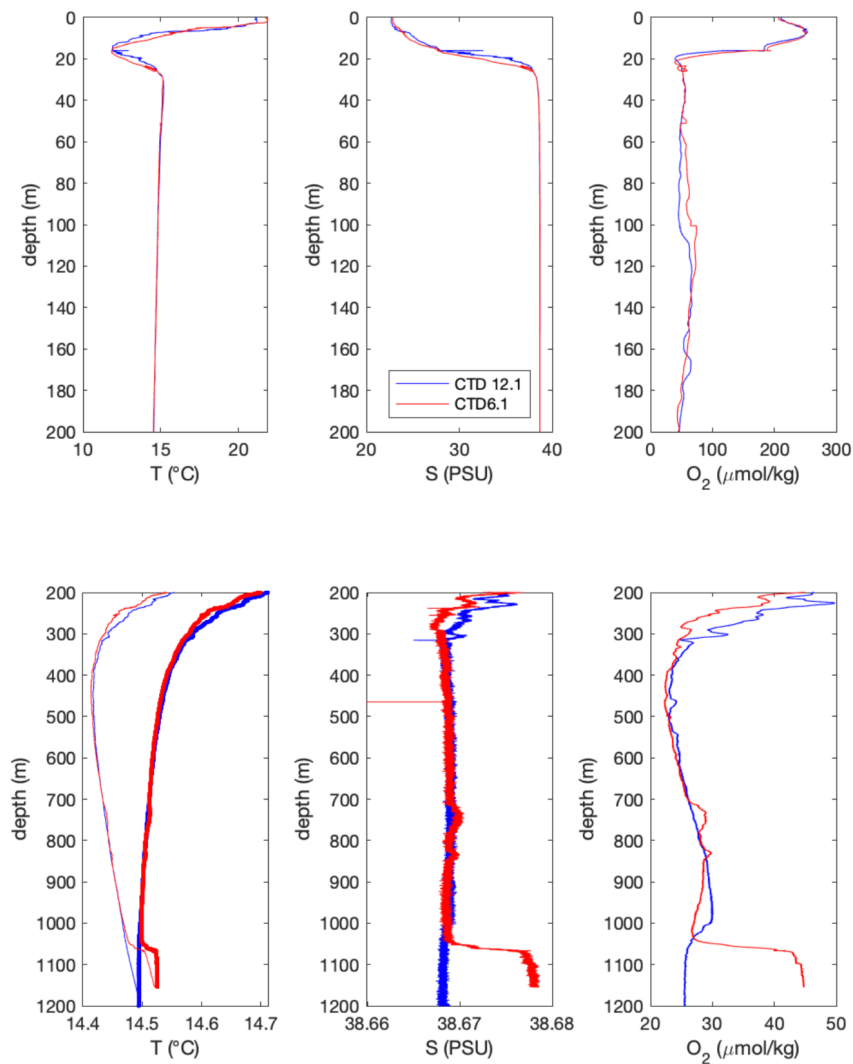
a supprimé: layer

a supprimé: However,

a supprimé: 4

a supprimé: 4

a supprimé: potential



676

677 **Figure 8.** Depth plots of Temperature (°C), Salinity (PSU) and oxygen concentration
 678 (μmol/kg) from CTD profiles acquired in the Sea of Marmara in June 2007 during
 679 Marnaut cruise of Ifremer RV L'Atalante (Henry et al., 2007). On the lower
 680 temperature plot, thin lines are measured values and thick lines are conservative
 681 temperatures calculated at 1180 m. Locations are shown on Figure 1

682

a supprimé: potential

4. Interpretation and discussion

4.1. Sequence of events

Let us first consider the potential influence of meteorology on the events recorded at the seafloor. Reanalysed ERA5 hourly wind and pressure data (Hersbach et al., 2018) interpolated at the location of the instrument indicate relatively low wind (less than 5 m/s) at the time of the earthquakes and during the hydrodynamic disturbances that followed (Figure 5). It is thus unlikely that wind influenced the course of these events. On the other hand, the current event on 20/09/2022 occurs at a time of high wind and follows a change of wind direction. Hypothetically, wind forcing may have caused this event, but probably not through sediment resuspension as acoustic backscatter remained low. A possible influence of wind on the motion of turbid clouds passing over the instrument after October 2 remains open for discussion.

The observations at the seafloor provide some insight on the complex sequence of events that followed the earthquakes and suggest the following scenarios. After the M_w 4.7 09/24/2019 a turbid cloud formed east of the instrument and drifted slowly. Considering the maximum velocity of the current (less than 4 cm/s) and the 4-hour interval between the earthquake and the passing of the turbid cloud over the instrument, the front of turbid water should have formed East North East of the instrument at a maximum distance of about 500 m, and this coincides with the base of the northern slope near the outlet of the canyon. Small scale failures on the steeper slopes on the sides of the canyon and shaking are possible causes of sediment resuspension. The clouds subsequently drifted downslope over a total horizontal distance of at most 1 kilometers before dissipating, adding the 500 m estimate above to the drift calculated after the passing of the front over the instrument (Figure 6).

The M_w 5.8 09/26/1919 caused stronger currents and a small temperature perturbation. Temperature records from turbidity currents invariably display a correlation between current onset and temperature change and this temperature change is nearly always positive (Mikada et al., 2006; Palanques et al., 2008; Kasaya et al., 2009; Xu et al., 2010; Khrpounoff et al., 2012; Liu et al., 2012; Hughes Clarke et al., 2006; Johnson et al., 2017; Brizuela et al., 2019; Normandeau et al., 2020; Heerema et al., 2022). Temperature spikes may thus be used to infer turbidity current occurrences and provenance (Johnson et al., 2017). That the currents we observe are associated with a temperature decrease rules out that they initiated at the shelf edge

a mis en forme : Titre 2, Sans numérotation ni puces

a supprimé: Inferred sequence of events

a mis en forme : Police :(Par défaut) Arial

a supprimé: se

a supprimé: s

a supprimé: NE

a supprimé: It is suspected that instability on the steeper slopes on the sides of the canyon is the primary cause of sediment suspension

a supprimé: much

725 as water above 600 m depth is at a higher potential temperature (temperature
726 corrected for the adiabatic gradient) than water at the seafloor (Figure 8). Water may
727 have been mixed locally or flowed down some distance down the slope. For instance,
728 currents may have originated from above the earthquake rupture zone, where the
729 seafloor lies in the 600-to-1200 m depth range.

730 The temperature records also concur with the current record to indicate that
731 currents in the water column remained moderate for several hours after the earthquake
732 and are not the primary cause of instrument tilting. First of all, there is a delay of at
733 least one hour after the earthquake (30 minutes after the tilting event) before
734 temperature starts decreasing significantly. Moreover, an acceleration of the
735 temperature rate of variation correlates with an increase in measured current speed
736 (to about 6 cm/s) between 14h and 15h (about 2 hours later), indicating that the tilted
737 current meter and the temperature sensors are providing concordant information.
738 Even if a short burst of current may have been missed because of the 1 hour interval
739 between current records, this would not explain why the frame remained stable in a
740 tilted position for several hours. Local liquefaction of the sediment beneath the device
741 is also an unlikely cause because the tilting of the instrument occurred 25 minutes after
742 the earthquake. A thin dense flow of remobilized sediment originating from the basin
743 slopes thus appears as a more likely cause. Partial burial of the device is attested by
744 presence of sandy mud caked on the device in various places: on the frame feet, on
745 the acoustic releases, on the optode connector and, also inside the plastic protection
746 of a flotation sphere from which bindings were broken. On the other hand, the current
747 speed of at least 25 cm/s recorded before the time when the device straightened up is
748 strong enough to cause erosion of mud deposits. It may thus be hypothesized that
749 erosion freed the device from the mud cover. The flotation spheres on the frame and
750 the concrete ballast at its base exert a moment that should keep the assembly stable
751 in an upright position unless the frame is loaded with sediment.

752 Powerful turbidity currents driven by dense basal flows have notably been
753 observed in Monterey Canyon (Paull et al., 2018) and may share some characteristics
754 with the event reported here, although this event is much weaker. These dense flows
755 are relatively thin (< 2 m in the Monterey Canyon case) and have the ability to displace
756 instruments before the development of turbulence in the water column. It appears likely
757 that, after the passing of the seismic wave, failures on slopes adjacent to the
758 deployment site caused a debris flow or dense mud flow that spread on the basin floor

a supprimé: .

a mis en forme : Non Surlignage

a mis en forme : Non Surlignage

a mis en forme : Non Surlignage

760 causing the tilting of the instrument and bottom water turbidity while turbulence in the
761 water column remained limited. As the base of the nearest slope is about 400 m north
762 of the instrument, this would imply a minimum velocity of 20 cm/s for the mudflow to
763 reach the device location in 25 minutes.

764 During the following 10 hours, the current record is incomplete but indicates
765 variations in strength and direction. One possible explanation is that widespread slope
766 instabilities triggered by the earthquake have resulted in several turbidity currents
767 recorded as successive pulses. Other possible explanations include oscillatory currents.
768 However, the role of seiches and surface gravity waves can be ruled out as no tsunami
769 was recorded by near shore tidal gauges around the Sea of Marmara. The relationship
770 between gravity wave amplitude A and bottom current amplitude U in the shallow water
771 linear approximation is given by $U=(g/H)^{1/2}A$, where H is water column height. An
772 oscillatory current of 10 cm/s at 1200 m depth would thus correspond to a free surface
773 oscillation of 1 m (or 100 hPa) for a standing wave (seiche) as well as a progressive
774 wave (tsunami). This should have been easily detected in a sea where tidal amplitude
775 is about 10 cm (Alpar and Yüce, 1998). The influence of baroclinic internal waves on
776 the halocline at 20-30 m depth must also be ruled out as they cannot physically
777 produce currents of more than a few cm/s at 1200 m. Nevertheless, it remains possible
778 that the interface at the top of the turbid cloud is affected by baroclinic waves.

779 The strongest current is recorded after 10 hours, which suggests that a turbidity
780 current initiated further upslope (but deeper than 600 m) may have reached the site
781 after a longer delay but may also have gained more kinetic energy on its downhill path.
782 This event, reaching a speed exceeding 25 cm/s apparently caused enough erosion
783 to free the device from the mud accumulation. The current then stabilizes in a westward
784 direction and decays progressively over the next 9 hours, which suggests the tail of a
785 turbidity current flowing in the canyon E of the deployment site has been recorded. The
786 hours-long delay between the earthquake and the passing of the fastest current over
787 the instrument may hypothetically correspond to the time for the head of the turbidity
788 current to travel from its source to the location of the instrument. Alternatively, a
789 sequence of slope failures may have lasted up to several hours after the earthquake.
790 Longer delays between loading events and turbidity currents, of several days to,
791 possibly, months, have been observed after floods (Carter et al., 2012) or after distant
792 earthquakes (Johnson et al., 2017). Another possibility is delayed ignition, which may
793 occur if the turbidity current develops from the hydrodynamic instability of a dilute turbid

a supprimé: After the passing of the seismic wave, triggering of instability on slopes adjacent to the deployment site caused mud flows that spread on the basin floor causing the tilting of the instrument 25 minutes after the earthquake, and bottom water turbidity. As the base of the nearest slope is about 400 m north of the instrument, this would imply a minimum velocity of 20 cm/s for the mudflow to reach the device location in 25 minutes.

a supprimé: W

a supprimé: may

a supprimé: T

a supprimé: in sediment resuspension

a supprimé: However,

a mis en forme : Ne pas vérifier l'orthographe ou la grammaire

a supprimé:

a supprimé: The length of the canyon valley between the device location and the 400 m isobath, inferred to be the minimum depth of the turbid water source, is about 13 km. In this scenario, the average velocity of the head of the turbidity current would be 30-40 cm/s.

a déplacé (et inséré) [4]

a supprimé: indirectly

cloud, indirectly resulting from slope failures and/or ground shaking (Parker, 1982; Mulder and Cochonnat, 1996; Piper and Normark, 2009; Hage et al., 2019).

a supprimé: rather than by acceleration of a dense mud flow

a supprimé: ¶

The distance travelled by the turbidity current on the basin floor cannot be accurately estimated with a single instrumental record. However the drift plot (Figure 6) obtained during the waning phase may be roughly indicative of the distance over which particles have been transported beyond the instrument by the turbidity current.

The drift distance is 3.5 km, and, when plotted over the bathymetric map, the drift appears to stay within the depositional fan at the outlet of the cayon, the extension of which is known from sediment sounder profiles (Figure 1). These calculations are only a rough estimate of the distance travelled by suspended particles as only the velocity at 1.5 m above the seafloor is known, and at a single point. Nevertheless, considering that the current strength will decrease with distance on the flat seafloor of the basin, it appears unlikely that sediments spread all over the 15x20 km basin floor as this would require velocities of the order of 1m/s, sustained over a wide area for several hours.

a supprimé:

a supprimé: The distance travelled by the turbidity current on the basin floor beyond the instrument may be estimated from the calculated drift during the waning phase, and is found to be about

a supprimé: (Figure 6). W

a supprimé: However,

The decay of the backscatter signal strength over the next three days may reflect the settling of sand size particles, likely clay aggregates, from a dilute suspension. This decay occurs in large part after the 9 hour waning phase of the turbidity current, while current velocity remains lower than 4 cm/s. For a first order assessment, Stokes settling velocity, an upper bound valid in dilute suspensions (e.g. Guazzelli and Morris, 2012) may be used. The Stokes settling velocity of 63 µm quartz grains (density 2650 kg/m³) in 13°C seawater is 2.7 mm/s, allowing such grains to drop by 700 m in three days. However, if the particles forming the cloud are mostly composed of clay aggregates, which density may be between 1200 and 1700 kg/m³, the settling velocity would be comprised between 0.3 mm and 1 mm/s. In this case the height of the suspended particle cloud could range between 70 and 250 m.

a supprimé: 3

a supprimé:

a supprimé: particles

a supprimé: put in suspension in the water column

a supprimé: after

a supprimé: this sequence of events

a supprimé: 3

a supprimé: comprised

4.2. Current observations across the earthquake magnitude range

In this study a seafloor device located at the outlet of a canyon in the Central Basin in the Sea of Marmara recorded a range of turbid events and currents induced by earthquakes that has been rarely documented. In September 2019, M_w 4.7 and 5.8 earthquakes occurred at a 5 km distance from the device as well as a series of smaller foreshocks and aftershocks. In this setting, earthquakes of magnitude less than 4 did not cause noticeable water column turbidity nor currents. The M_w 4.7 earthquake

a mis en forme : Hiérarchisation + Niveau : 2 + Style de numérotation : 1, 2, 3, ... + Commencer à : 1 + Alignement : Gauche + Alignement : 1.27 cm + Retrait : 2.29 cm

a supprimé: ¶
Discussion and conclusion¶

a supprimé: Data obtained

a supprimé: with

a supprimé:

a supprimé: bring some insight on how earthquakes scale with their hydrodynamic consequences

873 generated a turbid cloud on slopes a few hundred meters from the instrument and the
 874 cloud took 3-4 hours to drift down to the instrument location and 10 more hours to
 875 dissipate. As the current velocity remained small (less than 4 cm/s), it can be concluded
 876 that this cloud did not evolve into a self-sustained turbidity current (Parker, 1982). The
 877 M_w 5.8 earthquake initiated a turbidity current and the data obtained may be compared
 878 with more complete records obtained elsewhere with ADCP deployments and/or water
 879 column mooring lines. A velocity of several tens of centimeter per second is
 880 representative of the slower recorded examples, corresponding to mud rich flows
 881 associated with hyperpycnal flows or small landslides (Khripounoff et al. 2012), or to
 882 the smaller storm-related events (Normandeau et al., 2019). The event recorded is a
 883 very weak event compared to turbidity currents that followed large earthquakes or large
 884 slope instabilities. Cable breaks shows that the turbidity current triggered by the Grand
 885 Banks 1929 earthquake, M_s 7.2, reached velocities of at least 19 m/s (Piper et al.,
 886 1999). Velocity of turbidity currents estimated from cable breaks in the Gaoping
 887 Canyon and Manila Trench system range 5.5-12.7 m/s for the M_L 7.0 Pingtung
 888 earthquake in 2006 and 5.9-7.9 m/s for a M_L 6.4 earthquake (Gavey et al., 2017). From
 889 instrumental records, velocities of 2-7 m/s were reported for the turbidity current
 890 following Tohoku M_w 9.1 earthquake (Arai et al., 2013) and 1.4 m/s in the Tokachi-Oki
 891 M_w 8.3 case (Mikada et al., 2006). The downward current after the off-Izu Peninsula
 892 earthquake may be constrained with a noisy ADCP record to a maximum of 10-15 cm/s
 893 in a 20-30 m layer above the seafloor and lasted about one hour, peaking about 30
 894 minutes after the earthquake (Kasaya et al., 2009). This turbidity current thus appears
 895 less intense and shorter in duration than the one recorded in the Sea of Marmara, but
 896 the triggering earthquake was probably smaller (M 5.4 compared to M_w 5.8) and more
 897 distant (10 km). Moreover, the off-Izu event shares an important characteristic with the
 898 Sea of Marmara one in that the turbid cloud is observed to form some time before
 899 current builds up in the water column. When the maximum velocities reported are
 900 plotted against magnitude (Figure 9), they show a tendency for larger earthquakes to
 901 trigger stronger currents, which is hardly surprising. It also appears that estimates from
 902 cable breaks tend to give higher value than instrumental records. This may perhaps
 903 be because instruments give the maximum current speed at a single position while
 904 cable breaks yield an integrated estimation of maximum current speed. Moreover, if
 905 cable breaks are caused by a dense basal flow, it is yet unclear how its speed relates
 906 to that of currents in the water column (Paul et al., 2018). The data set available today

a supprimé: of turbidity currents

a supprimé: The duration of the event in the Sea of Marmara (about 10 hours) appear fairly typical and comparable with events recorded in other locations regardless of the initiation mechanism, which comprise hyperpycnal flows from river floods (Var and Gaoping canyons), storm waves and dredging (Gulf of St Laurence and Monterey canyon), and slope instabilities triggered by an earthquake (Tokachi-oki) or by other processes (Var canyon) (Normandeau et al., 2019; Khripounoff et al., 2012; Xu et al., 2004; Liu et al., 2012; Mikada et al., 2006). Longer duration events with very different hydrodynamic characteristics have been observed in larger scale systems (e.g. Congo deep sea canyon, Azpiroz-Zabala et al., 2017). On the other hand, events recorded closer to shore on the edge of the continental shelf or on a delta front have much shorter durations (Xu et al., 2010; Hughes Clarke, 2016). In events of comparable scale to the Sea of Marmara one, the velocity of the current generally reaches its maximum several meters above the seafloor, so that the velocity recorded by our instrument at 1.5 m from the seafloor is within the boundary layer, and lower than either the maximum current velocity or the velocity of the head of the turbidity current.

a supprimé: , to the

a supprimé: er

a supprimé: T

a supprimé: es

a supprimé: ing

a supprimé: have reached maximum velocities of 20 m/s

a mis en forme : Indice

a supprimé:

a mis en forme : Indice

a mis en forme : Indice

a supprimé: V

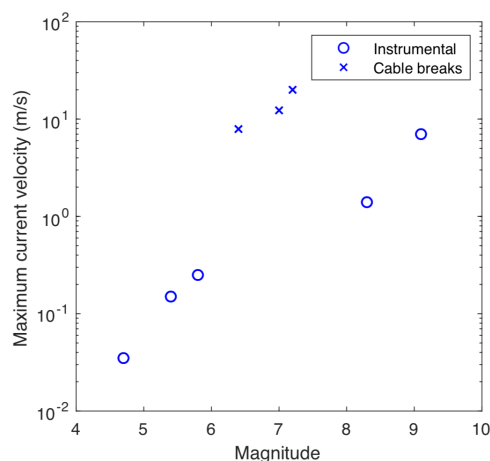
a mis en forme : Indice

a supprimé: also

a mis en forme : Indice

a supprimé:

remains insufficient to reach general conclusions regarding scaling, and other factors than earthquake magnitude, such as slope, would need to be taken into account.



a supprimé: These observations suggest that a general scaling relationship could exist between earthquake magnitudes and the strength and extent of the turbidity currents they induce. Moreover, although the off-Izu event is shorter than the Sea of Marmara one, they share an important characteristic in that the turbid cloud is observed to form when a mud flow hits the observatory site and some time before current builds up in the water column.

Figure 9. Maximum measured current velocity as a function of earthquake magnitude for the cases discussed in text.

4.3. Implications for sediment transport after earthquakes

Several observations from the monitoring records have special relevance for the understanding of sediment resuspension and transport processes during earthquakes. The first one is that earthquakes can induce sediment resuspension in situations where current remains too low to be the primary cause or resuspension. This is apparent when comparing events on Sept 20 (unrelated to earthquake and without turbidity) and Sept 24 (after M_w 4.7 earthquake and turbid) that have comparable current speeds. Resuspension may be an immediate effect of ground shaking or results from local slope failures. This process may be important as it opens the possibility of triggering turbidity currents after earthquakes by hydrodynamic instability within the water column. The second one is that a mass flow sufficiently strong and dense to displace a heavy instrument occurred at a time when there was no indication of advection in the water column. Currents in the water column apparently continued to increase in strength after this initial mass flow had stopped. A third observation is that the water displaced with the turbidity currents is deep water, as indicated by the temperature record. Likely, the displaced water originates from where the earthquake triggered sediment mobilization, that is in relatively deep water around the earthquake source area north and west of

a mis en forme : Titre 2, Gauche

a mis en forme : Indice

the instrument location (Figure 1). Turbidity currents more commonly originate from continental shelf edges or the upper part of continental slopes. This is notably the case when they are related to storms, river discharge or sediment loading. However, triggering by earthquakes may affect any part of the continental slope depending on the location of active faults. The case we reported shows that a moderate earthquake (M_w 5.8) can cause sediment remobilization near the base of the slope rather than at the shelf edge resulting in different flow dynamics than generally assumed for sediment remobilization events.

The geomorphological context of the deployment site also needs to be taken into account. It is located on a depositional fan at the outlet of a canyon and south of a slope identified as unstable from geomorphological criteria (Zitter et al., 2012). We have shown that a debris flow or dense mud flow originating from this unstable slope, followed several hours later by a turbidity current flowing along the canyon could well explain the sequence of event following the M_w 5.8 earthquake. Although this is not the only possible explanation for the observations, we believe it is the most likely one considering the geomorphological context. We estimated that the current during this event was probably too weak to spread a layer of sediment over the entire Central Basin floor. It is also unclear whether this event left on the fan a sedimentary layer that may be identified as a seismoturbidite, as a debris flow or as a layer of homogeneous mud. Differences between the fan and the basin in the number of sedimentary events and of their characteristics could explain why the sequence of seismic reflectors on sediment sounder profiles differs in the basin and in the fan (Figure 1). For all these reasons, the base of slope or canyon outlets are not good sampling locations for obtaining reliable earthquake records. In previous studies in the Sea of Marmara (e.g. McHugh et al., 2014), samples were taken across the basin depocenter for this purpose and events correlated between cores could also be correlated with historical earthquakes of estimated magnitude > 6.8 . This approach remains in principle valid.

5. Conclusion

Instrumental records obtained in the Sea of Marmara Central Basin near the base of an unstable slope and the outlet of a canyon bring some insight on sediment remobilization by proximal (≈ 5 km) earthquakes and their hydrodynamic consequences.

-The smaller earthquakes ($M_w < 4$) are not associated with water column events

a mis en forme : Indice

a supprimé: The 10 hours delay observed in the Sea of Marmara between the triggering event and the peak of the turbidity current is long compared to the 2 hours delay observed after Tohoku and Tokachi-oki earthquakes. We suggested earlier that the long delay may simply result from a slower velocity of the turbidity current or from delayed slope failure. Another possibility is delayed ignition, which may occur if the turbidity current develops indirectly from the hydrodynamic instability of a turbid cloud resulting from slope failures and/or ground shaking rather than by acceleration of a dense mud flow (Parker, 1982; Mulder and Cochonnat, 1996; Piper and Normark, 2009).

a déplacé vers le haut [4]: Another possibility is delayed ignition, which may occur if the turbidity current develops indirectly from the hydrodynamic instability of a turbid cloud resulting from slope failures and/or ground shaking rather than by acceleration of a dense mud flow (Parker, 1982; Mulder and Cochonnat, 1996; Piper and Normark, 2009).

a supprimé: The scenario we propose for the Sept 26, 2019 earthquake involving mud flows from proximal sources, followed by turbidity currents originating at larger distances, and the subsequent settling of sediment in suspension, could relate with the structure of turbidite-homogenites. Progressive or pulsed build-up of turbidity current energy is considered typical of hyperpycnal flows initiated by river floods (Mulder et al., 2003) but reverse grading and pulsing is also observed in seismoturbidites (Gutiérrez-Pastor et al., 2013). In the Sea of Marmara, many of the laminated turbidites sampled in Kumburgaz Basin formed from the amalgamation (below the homogenite layer) of at least two flows, the first one being finer and less sorted (Yakupoglu et al., 2019). The coarsening observed in this context is often associated with an increase of the calcium content indicative of a shallower source, rich in biogenic carbonate material. However, in the case observed in the present study, remobilization of sediment should be limited to the lower slope as th...

a supprimé: ,

a supprimé: and on a depositional fan at the outlet of a canyon is also consistent with the proposed scenario. We estimated by integrating recorded current velocity that the current during this event was not strong enough...

a supprimé: However, as hypothesized by previous studies (McHugh et al., 2014), turbidite-homogenite deposits that can be correlated between cores taken...

a supprimé: ,

a supprimé: which may

a supprimé:

a supprimé: Moreover, it is still unknown whether the Sept 26 event left a trace on the seafloor morphology and in the sediment record. Performing new core sampling and very high-resolution geophysical surveys...

a mis en forme : Hiérarchisation + Niveau : 1 + Style de numérotation : 1, 2, 3, ... + Commencer à : 1 + Alignement : Gauche + Alignement : 1.27 cm + Retrait : 2.03 cm

a supprimé: ¶

1111 -A $M_w = 4.7$ earthquake caused the formation of a turbid cloud and low currents
1112 not exceeding 4 cm/s.

1113 - A $M_w = 5.8$ earthquake at the same location caused a mass flow strong enough
1114 to capsize a heavy instrument. Subsequent movements of the water masses remained
1115 local, mixing deep waters at a scale of 5-to-10 km maximum.

1116 This suggests that a continuum of hydrodynamic events of increasing intensity
1117 with earthquake magnitude occur above a threshold, corresponding to $M_w \approx 4$ at the
1118 studied location. Moderate earthquakes can thus generate mass flows and turbidity
1119 currents of limited extension that may confuse paleoseismological records in cores
1120 taken near the edges of basins. However, the local nature of these events may help
1121 distinguish them from the consequences of storms and floods, expected to initiate from
1122 near the edge of the continental shelf. Performing new core studies and very high-
1123 resolution geophysical surveys in this area would thus have important implications for
1124 understanding under which conditions earthquakes leave a distinctive trace in the
1125 sediment record.

1126

1127 Acknowledgements

1128 Financial support was provided by the bilateral ANR/TÜBITAK collaborative research
1129 project MAREGAMI (ANR-16-CE03-0010-02 and Tübitak Project 116Y371) and by
1130 CNRS-INSU through the European Multidisciplinary Sea Observatory (EMSO)
1131 Research Infrastructure program. DT-INSU and Istanbul Technical University
1132 hydrodynamic engineering department provided technical support for device design,
1133 construction, and deployment. Bernard Mercier de Lépinay provided processed
1134 sediment sonar profiles. We thank the crew and Captain of R/V Yunus (Istanbul
1135 University) for their support during installation and recovery of the instruments.
1136 Seafloor monitoring data are available through SEANOE (Henry et al., 2021) and
1137 CTD profile data through SISMER Oceanographic Data portal (Henry et al., 2007).

1138

1139 References

1140 Adams, J. (1990). Paleoseismicity of the Cascadia Subduction Zone: Evidence from turbidites off the
1141 Oregon-Washington Margin. *Tectonics*, 9(4), 569–583.
1142 <https://doi.org/10.1029/TC009i004p00569>

a mis en forme : Indice

1143 Alpar, B., & Yüce, H. (1998). Sea-level variations and their interactions between the Black
1144 Sea and the Aegean Sea. *Estuarine, Coastal and Shelf Science*, 46, 609–619.

1145 Arai, K., Naruse, H., Miura, R., Kawamura, K., Hino, R., Ito, Y., Inazu, D., Yokokawa, M.,
1146 Izumi, N., Murayama, M., & Kasaya, T. (2013). Tsunami-generated turbidity current of
1147 the 2011 Tohoku-Oki earthquake. *Geology*, 41(11), 1195–1198.
1148 <https://doi.org/10.1130/G34777.1>

1149 [Atwater, B. F., Carson, B., Griggs, G. B., Johnson, P. P., & Salmi, M. S. \(2014\). Rethinking](#)
1150 [turbidite paleoseismology along the Cascadia subduction zone. *Geology*, 42\(9\), 827–](#)
1151 [830. <https://doi.org/10.1130/G35902.1>](#)

1152 Armijo, R., Meyer, B., Navarro, S., King, G., & Barka, A. (2002). Asymmetric slip partitioning
1153 in the Sea of Marmara pull-apart: a clue to propagation processes of the North Anatolian
1154 Fault? *Terra Nova*, 14(2), 80–86. <https://doi.org/10.1046/j.1365-3121.2002.00397.x>

1155 Armijo, R. and J. Malavieille (2002) MARMARASCARPS cruise, RV L'Atalante,
1156 <https://doi.org/10.17600/2010140>

1157 Azpiroz-Zabala, M., Cartigny, M. J. B., Talling, P. J., Parsons, D. R., Sumner, E. J., Clare, M.
1158 A., Simmons, S. M., Cooper, C., & Pope, E. L. (2017). Newly recognized turbidity current
1159 structure can explain prolonged flushing of submarine canyons. *Science Advances*,
1160 3(10). <https://doi.org/10.1126/sciadv.1700200>

1161 Beck, C., Mercier de Lépinay, B., Schneider, J. L., Cremer, M., Çağatay, N., Wendenbaum,
1162 E., et al. (2007). Late Quaternary co-seismic sedimentation in the Sea of Marmara's
1163 deep basins. *Sedimentary Geology*, 199, 65–89.
1164 <https://doi.org/10.1016/j.sedgeo.2005.12.031>

1165 Beşiktepe, Ş. T., Sur, H. İ., Özsoy, E., Latif, M. A., Oğuz, T., & Ünlüata, Ü. (1994). The
1166 circulation and hydrography of the Marmara Sea. *Progress in Oceanography*, 34(4),
1167 285–334. [https://doi.org/10.1016/0079-6611\(94\)90018-3](https://doi.org/10.1016/0079-6611(94)90018-3)

1168 [Bradley, B. A., Razafindrakoto, H. N. T., & Polak, V. \(2017\). Ground-Motion Observations](#)
1169 [from the 14 November 2016 Mw 7.8 Kaikoura, New Zealand, Earthquake and Insights](#)
1170 [from Broadband Simulations. *Seismological Research Letters*, 88\(3\), 740–756.](#)
1171 <https://doi.org/10.1785/0220160225>

1172 Brizuela, N., Filonov, A., & Alford, M. H. (2019). Internal tsunami waves transport sediment
1173 released by underwater landslides. *Scientific Reports*, 9(1), 10775.
1174 <https://doi.org/10.1038/s41598-019-47080-0>

1175 Bulut, F., Aktuğ, B., Yalıtırak, C., Doğru, A., & Özener, H. (2019). Magnitudes of future large
1176 earthquakes near Istanbul quantified from 1500 years of historical earthquakes, present-
1177 day microseismicity and GPS slip rates. *Tectonophysics*, 764(July 2018), 77–87.
1178 <https://doi.org/10.1016/j.tecto.2019.05.005>

- 1179 Çağatay, M. N., Erel, L., Bellucci, L. G., Polonia, a., Gasperini, L., Eriş, K. K., Sancar, Ü.,
1180 Biltekin, D., Uçarkuş, G., Ülgen, U. B., & Damci, E. (2012). Sedimentary earthquake
1181 records in the İzmit Gulf, Sea of Marmara, Turkey. *Sedimentary Geology*, 282, 347–359.
1182 <https://doi.org/10.1016/j.sedgeo.2012.10.001>
- 1183 Çağatay, N. M., Uçarkuş, G., Eris, K. K., Henry, P., Gasperini, L., & Polonia, A. (2015).
1184 Submarine canyons of the Sea of Marmara. In F. Briand (Ed.), *Submarine Canyon*
1185 *Dynamics in the Mediterranean and Tributary Seas*, CIESM Workshop Monograph n° 47
1186 (pp. 123–135). CIESM Publisher, Monaco. <https://doi.org/10.13140/RG.2.1.1692.8402>
- 1187 [Carter, L., Milliman, J. D., Talling, P. J., Gavey, R., & Wynn, R. B. \(2012\). Near-synchronous](https://doi.org/10.1029/2012GL051172)
1188 [and delayed initiation of long run-out submarine sediment flows from a record-breaking](https://doi.org/10.1029/2012GL051172)
1189 [river flood, offshore Taiwan. *Geophysical Research Letters*, 39\(12\), 6–10.](https://doi.org/10.1029/2012GL051172)
1190 <https://doi.org/10.1029/2012GL051172>
- 1191 Cattaneo, A., Babonneau, N., Ratzov, G., Dan-Unterseh, G., Yelles, K., Bracane, R., Mercier
1192 De Lapinay, B., Boudiaf, A., & Daverchare, J. (2012). Searching for the seafloor
1193 signature of the 21 May 2003 Boumerdes earthquake offshore central Algeria. *Natural*
1194 *Hazards and Earth System Science*, 12(7), 2159–2172. [https://doi.org/10.5194/nhess-](https://doi.org/10.5194/nhess-12-2159-2012)
1195 [12-2159-2012](https://doi.org/10.5194/nhess-12-2159-2012)
- 1196 Dan, G., Sultan, N., Savoye, B., Deverchere, J., & Yelles, K. (2009). Quantifying the role of
1197 sandy-silty sediments in generating slope failures during earthquakes: Example from the
1198 Algerian margin. *International Journal of Earth Sciences*, 98(4), 769–789.
1199 <https://doi.org/10.1007/s00531-008-0373-5>
- 1200 Drab, L., Hubert Ferrari, A., Schmidt, S., & Martinez, P. (2012). The earthquake sedimentary
1201 record in the western part of the Sea of Marmara, Turkey. *Natural Hazards and Earth*
1202 *System Science*, 12(4), 1235–1254. <https://doi.org/10.5194/nhess-12-1235-2012>
- 1203 Drab, L., Hubert-Ferrari, A., Schmidt, S., Martinez, P., Carlut, J., & El Ouahabi, M. (2015).
1204 Submarine Earthquake History of the Çınarcık Segment of the North Anatolian Fault in
1205 the Marmara Sea, Turkey. *Bulletin of the Seismological Society of America*, 105(2A),
1206 622–645. <https://doi.org/10.1785/0120130083>
- 1207 Eriş, K. K., Çağatay, N., Beck, C., Mercier de Lepinay, B., & Corina, C. (2012). Late-
1208 Pleistocene to Holocene sedimentary fills of the Çınarcık Basin of the Sea of Marmara.
1209 *Sedimentary Geology*, 281, 151–165. <https://doi.org/10.1016/j.sedgeo.2012.09.001>
- 1210 Garfield, N., Rago, T. A., Schnebele, K. J., & Collins, C. A. (1994). Evidence of a turbidity
1211 current in Monterey Submarine Canyon associated with the 1989 Loma Prieta
1212 earthquake. *Continental Shelf Research*, 14(6), 673–686. [https://doi.org/10.1016/0278-](https://doi.org/10.1016/0278-4343(94)90112-0)
1213 [4343\(94\)90112-0](https://doi.org/10.1016/0278-4343(94)90112-0)
- 1214 [Gavey, R., Carter, L., Liu, J. T., Talling, P. J., Hsu, R., Pope, E., & Evans, G. \(2017\).](https://doi.org/10.1016/0278-4343(94)90112-0)
1215 [Frequent sediment density flows during 2006 to 2015, triggered by competing seismic](https://doi.org/10.1016/0278-4343(94)90112-0)

1216 [and weather events: Observations from subsea cable breaks off southern Taiwan.](#)
1217 [Marine Geology, 384, 147–158. <https://doi.org/10.1016/j.margeo.2016.06.001>](#)
1218 Goldfinger, C., Nelson, C. H., & Johnson, J. E. (2003). Holocene earthquake records from
1219 the cascadia subduction zone and northern san andreas fault based on precise dating of
1220 offshore turbidites. *Annual Review of Earth and Planetary Sciences*, 31(1), 555–577.
1221 <https://doi.org/10.1146/annurev.earth.31.100901.141246>
1222 Goldfinger, C., Nelson, C. H., Morey, A. E., Johnson, J. E., Patton, J., Karabanov, E.,
1223 Gutiérrez-Pastor, J., Eriksson, A. T., Gràcia, E., Dunhill, G., Enkin, R. J., Dallimore, A., &
1224 Vallier, T. (2012). Earthquake Hazards of the Pacific Northwest Coastal and Marine
1225 Regions Turbidite Event History — Methods and Implications for Holocene
1226 Paleoseismicity of the Cascadia Subduction Zone Professional Paper 1661 – F. USGS,
1227 Professional Paper 1661-F, 170. Retrieved from <http://pubs.usgs.gov/pppp1661f/>
1228 Grall, C., Henry, P., Tezcan, D., Mercier de Lepinay, B., Becel, A., Geli, L., Rudkiewicz, J.-L.,
1229 Zitter, T., & Harnegnies, F. (2012). Heat flow in the Sea of Marmara Central Basin:
1230 Possible implications for the tectonic evolution of the North Anatolian fault. *Geology*,
1231 40(1), 3–6. <https://doi.org/10.1130/G32192.1>
1232 Guazzelli, E., Morris, J. F., & Pic, S. (2011). A Physical Introduction to Suspension
1233 Dynamics. Cambridge: Cambridge University Press.
1234 <https://doi.org/10.1017/CBO9780511894671>
1235 Guerrero, M., Rüther, N., & Szupiany, R. N. (2012). Laboratory validation of acoustic Doppler
1236 current profiler (ADCP) techniques for suspended sediment investigations. *Flow*
1237 *Measurement and Instrumentation*, 23(1), 40–48.
1238 <https://doi.org/10.1016/j.flowmeasinst.2011.10.003>
1239 Guerrero, M., Szupiany, R. N., & Amsler, M. (2011). Comparison of acoustic backscattering
1240 techniques for suspended sediments investigation. *Flow Measurement and*
1241 *Instrumentation*, 22(5), 392–401. <https://doi.org/10.1016/j.flowmeasinst.2011.06.003>
1242 Gutiérrez-Pastor, J., Nelson, C. H., Goldfinger, C., & Escutia, C. (2013). Sedimentology of
1243 seismo-turbidites off the Cascadia and northern California active tectonic continental
1244 margins, northwest Pacific Ocean. *Marine Geology*, 336, 99–119.
1245 <https://doi.org/10.1016/j.margeo.2012.11.010>
1246 [Gwyn Lintern, D., Hill, P. R., & Stacey, C. \(2016\). Powerful unconfined turbidity current](#)
1247 [captured by cabled observatory on the fraser river delta slope, British Columbia, Canada.](#)
1248 [Sedimentology, 63\(5\), 1041–1064. <https://doi.org/10.1111/sed.12262>](#)
1249 [Hage, S., Cartigny, M. J. B., Sumner, E. J., Clare, M. A., Hughes Clarke, J. E., Talling, P. J.,](#)
1250 [et al. \(2019\). Direct Monitoring Reveals Initiation of Turbidity Currents From Extremely](#)
1251 [Dilute River Plumes. *Geophysical Research Letters*, 46\(20\), 11310–11320.](#)
1252 <https://doi.org/10.1029/2019GL084526>

a supprimé: ¶

Hébert, H., Schindelé, F., Altinok, Y., Alpar, B., & Gazioglu, C. (2005). Tsunami hazard in the Marmara Sea (Turkey): A numerical approach to discuss active faulting and impact on the Istanbul coastal areas. *Marine Geology*, 215, 23–43. <https://doi.org/10.1016/j.margeo.2004.11.006>

Heezen, B. C., Ericson, D. B., & Ewing, M. (1954). Further evidence for a turbidity current following the 1929 Grand banks earthquake. *Deep Sea Research* (1953), 1(4), 193–202. [https://doi.org/10.1016/0146-6313\(54\)90001-5](https://doi.org/10.1016/0146-6313(54)90001-5)

[Heerema, C. J., Cartigny, M. J. B., Jacinto, R. S., Simmons, S. M., Apprioual, R., & Talling, P. J. \(2022\). How distinctive are flood-triggered turbidity currents? *Journal of Sedimentary Research*, 92\(1\), 1–11. <https://doi.org/10.2110/jsr.2020.168>](#)

Henry, P., A.M.C. Şengör, M.N. Çağatay (2007) MARNAUT cruise, RV L'Atalante, <https://doi.org/10.17600/7010070>

Henry, P., Özeren M.S., Desprez De Gesincourt O., de Saint-Leger E., Libes., M., Çakir, Z., Yakupoğlu, N., Géli, L. (2021). EMSO / MAREGAMI Marmara bottom pressure and current records. SEANOE. <https://doi.org/10.17882/78928>

[Hersbach, H., Bell, B., Berrisford, P., Biavati, G., Horányi, A., Muñoz Sabater, J., Nicolas, J., Peubey, C., Radu, R., Rozum, I., Schepers, D., Simmons, A., Soci, C., Dee, D., Thépaut, J.-N. \(2018\): ERA5 hourly data on single levels from 1959 to present. Copernicus Climate Change Service \(C3S\) Climate Data Store \(CDS\).](#) <https://doi.org/10.24381/cds.adbb2d47>

[Howarth, J. D., Orpin, A. R., Kaneko, Y., Strachan, L. J., Nodder, S. D., Mountjoy, J. J., Barnes, P. M., Bostock, H. C., Holden, C., Jones, K., & Çağatay, M. N. \(2021\). Calibrating the marine turbidity palaeoseismometer using the 2016 Kaikōura earthquake. *Nature Geoscience*, 14\(3\), 161–167. <https://doi.org/10.1038/s41561-021-00692-6>](#)

Hsu, S. K., Kuo, J., Lo, C. L., Tsai, C. H., Doo, W. Bin, Ku, C. Y., & Sibuet, J. C. (2008). Turbidity currents, submarine landslides and the 2006 Pingtung earthquake off SW Taiwan. *Terrestrial, Atmospheric and Oceanic Sciences*, 19(6), 767–772. [https://doi.org/10.3319/TAO.2008.19.6.767\(PT\)](https://doi.org/10.3319/TAO.2008.19.6.767(PT))

Hughes Clarke, J. E. (2016). First wide-angle view of channelized turbidity currents links migrating cyclic steps to flow characteristics. *Nature Communications*, 7(1), 11896. <https://doi.org/10.1038/ncomms11896>

Ikehara, K., Kanamatsu, T., Nagahashi, Y., Strasser, M., Fink, H., Usami, K., et al. (2016). Documenting large earthquakes similar to the 2011 Tohoku-oki earthquake from sediments deposited in the Japan Trench over the past 1500 years. *Earth and Planetary Science Letters*, 445, 48–56. doi:10.1016/j.epsl.2016.04.009

Johnson, H. P., Gomberg, J. S., Hautala, S. L., & Salmi, M. S. (2017). Sediment gravity flows triggered by remotely generated earthquake waves. *Journal of Geophysical Research: Solid Earth*, 122(6), 4584–4600. <https://doi.org/10.1002/2016JB013689>

Karabulut, H., Güvercin, S. E., Eskikoç, F., Konca, A. Ö., & Ergintav, S. (2021). The moderate size 2019 September Mw5.8 Silivri earthquake unveils the complexity of the Main Marmara Fault shear zone. *Geophysical Journal International*, 224(1), 377–388. <https://doi.org/10.1093/gji/ggaa469>

Kasaya, T., Mitsuzawa, K., Goto, T., Iwase, R., Sayanagi, K., Araki, E., Asakawa, K., Mikada, H., Watanabe, T., Takahashi, I., & Nagao, T. (2009). Trial of Multidisciplinary Observation at an Expandable Sub-Marine Cabled Station “Off-Hatsushima Island Observatory” in Sagami Bay, Japan. *Sensors*, 9(11), 9241–9254. <https://doi.org/10.3390/s91109241>

Khripounoff, A., Crassous, P., Lo Bue, N., Dennielou, B., & Silva Jacinto, R. (2012). Different types of sediment gravity flows detected in the Var submarine canyon (northwestern Mediterranean Sea). *Progress in Oceanography*, 106, 138–153. <https://doi.org/10.1016/j.pocean.2012.09.001>

Le Pichon, X., Chamot-Rooke, N., Rangin, C., & Sengör, A. M. C. (2003). The North Anatolian fault in the Sea of Marmara. *Journal of Geophysical Research*, 108, 2179. <https://doi.org/10.1029/2002JB001862>

Le Pichon, X., Şengör, A. M. C., Demirbağ, E., Rangin, C., İmren, C., Armijo, R., Görür, N., Çağatay, N., Mercier de Lepinay, B., Meyer, B., Saatçılar, R., & Tok, B. (2001). The active Main Marmara Fault. *Earth and Planetary Science Letters*, 192(4), 595–616. [https://doi.org/10.1016/S0012-821X\(01\)00449-6](https://doi.org/10.1016/S0012-821X(01)00449-6)

Liu, J. T., Wang, Y.-H., Yang, R. J., Hsu, R. T., Kao, S.-J., Lin, H.-L., & Kuo, F. H. (2012). Cyclone-induced hyperpycnal turbidity currents in a submarine canyon. *Journal of Geophysical Research: Oceans*, 117(C4), n/a-n/a. <https://doi.org/10.1029/2011JC007630>

McDougall, T. J., & Barker, P. M. (2011). *Getting started with TEOS-10 and the Gibbs Seawater (GSW) oceanographic toolbox. Scor/lapso WG*, 127, 1-28.

McDougall, T. J., Feistel, R., & Pawlowicz, R. (2013). *Thermodynamics of Seawater. In International Geophysics (2nd ed., Vol. 103, pp. 141–158). Elsevier Ltd.* <https://doi.org/10.1016/B978-0-12-391851-2.00006-4>

McHugh, C. M. G., Seeber, L., Cormier, M. H., Dutton, J., Çağatay, N., Polonia, A., Ryan, W. B. F., & Görür, N. (2006). Submarine earthquake geology along the North Anatolia Fault in the Marmara Sea, Turkey: A model for transform basin sedimentation. *Earth and Planetary Science Letters*, 248, 661–684. <https://doi.org/10.1016/j.epsl.2006.05.038>

a mis en forme : Police :(Par défaut) Arial

1325 McHugh, C. M., Seeber, L., Braudy, N., Cormier, M. H., Davis, M. B., Diebold, J. B.,
 1326 Dieudonne, N., Douilly, R., Gulick, S. P. S., Hornbach, M. J., Johnson, H. E., Mishkin, K.
 1327 R., Sorlien, C. C., Steckler, M. S., Symithe, S. J., & Templeton, J. (2011). Offshore
 1328 sedimentary effects of the 12 January 2010 Haiti earthquake. *Geology*, 39(8), 723–726.
 1329 <https://doi.org/10.1130/G31815.1>
 1330 McHugh, C. M. G., Braudy, N., Çağatay, M. N., Sorlien, C., Cormier, M.-H., Seeber, L., &
 1331 Henry, P. (2014). Seafloor fault ruptures along the North Anatolia Fault in the Marmara
 1332 Sea, Turkey: Link with the adjacent basin turbidite record. *Marine Geology*, 353, 65–83.
 1333 <https://doi.org/10.1016/j.margeo.2014.03.005>
 1334 Mikada, H., Mitsuzawa, K., Matsumoto, H., Watanabe, T., Morita, S., Otsuka, R., Sugioka,
 1335 H., Baba, T., Araki, E., & Suyehiro, K. (2006). New discoveries in dynamics of an M8
 1336 earthquake-phenomena and their implications from the 2003 Tokachi-oki earthquake
 1337 using a long term monitoring cabled observatory. *Tectonophysics*, 426(1–2), 95–105.
 1338 <https://doi.org/10.1016/j.tecto.2006.02.021>
 1339 [Mountjoy, J. J., Howarth, J. D., Orpin, A. R., Barnes, P. M., Bowden, D. A., Rowden, A. A.,](#)
 1340 [Schimel, A. C. G., Holden, C., Horgan, H. J., Nodder, S. D., Patton, J. R., Lamarche, G.,](#)
 1341 [Gerstenberger, M., Micallef, A., Pallentin, A., & Kane, T. \(2018\). Earthquakes drive large-](#)
 1342 [scale submarine canyon development and sediment supply to deep-ocean basins.](#)
 1343 [Science Advances, 4\(3\), 1–9. https://doi.org/10.1126/sciadv.aar3748](#)
 1344 Mulder, T., & Cochonnat, P. (1996). Classification of Offshore Mass Movements. *SEPM*
 1345 *Journal of Sedimentary Research*, Vol. 66. <https://doi.org/10.1306/D42682AC-2B26->
 1346 [11D7-8648000102C1865D](https://doi.org/10.1306/D42682AC-2B26-11D7-8648000102C1865D)
 1347 Mulder, T., Syvitski, J. P. M., Migeon, S., Faugères, J.-C., & Savoye, B. (2003). Marine
 1348 hyperpynal flows: initiation, behavior and related deposits. A review. *Marine and*
 1349 *Petroleum Geology*, 20(6–8), 861–882. <https://doi.org/10.1016/j.marpetgeo.2003.01.003>
 1350 Nakajima, T., & Kanai, Y. (2000). Sedimentary features of seismoturbidites triggered by the
 1351 1983 and older historical earthquakes in the eastern margin of the Japan Sea.
 1352 *Sedimentary Geology*, 135(1–4), 1–19. [https://doi.org/10.1016/S0037-0738\(00\)00059-2](https://doi.org/10.1016/S0037-0738(00)00059-2)
 1353 Normandeau, A., Bourgault, D., Neumeier, U., Lajeunesse, P., St-Onge, G., Gostiaux, L., &
 1354 Chavanne, C. (2020). Storm-induced turbidity currents on a sediment-starved shelf:
 1355 Insight from direct monitoring and repeat seabed mapping of upslope migrating
 1356 bedforms. *Sedimentology*, 67(2), 1045–1068. <https://doi.org/10.1111/sed.12673>
 1357 Okal, E. A., & Synolakis, C. E. (2001). Comment on “Origin of the 17 July 1998 Papua New
 1358 Guinea Tsunami: Earthquake or Landslide?” by E. L. Geist. *Seismological Research*
 1359 *Letters*, 72(3), 362–366. <https://doi.org/10.1785/gssrl.72.3.362>
 1360 Özeren, M. S., Çağatay, M. N., Postacioğlu, N., Şengör, a. M. C., Görür, N., & Eriş, K.
 1361 (2010). Mathematical modelling of a potential tsunami associated with a late glacial

submarine landslide in the Sea of Marmara. *Geo-Marine Letters*, 30, 523–539.
<https://doi.org/10.1007/s00367-010-0191-1>

Palanques, A., Guillén, J., Puig, P., & Durrieu de Madron, X. (2008). Storm-driven shelf-to-canyon suspended sediment transport at the southwestern Gulf of Lions. *Continental Shelf Research*, 28(15), 1947–1956. <https://doi.org/10.1016/j.csr.2008.03.020>

Parker, G. (1982). Conditions for the ignition of catastrophically erosive turbidity currents. *Marine Geology*, 46(3–4), 307–327. [https://doi.org/10.1016/0025-3227\(82\)90086-X](https://doi.org/10.1016/0025-3227(82)90086-X)

Paull, C. K., Talling, P. J., Maier, K. L., Parsons, D., Xu, J., Caress, D. W., et al. (2018). Powerful turbidity currents driven by dense basal layers. *Nature Communications*, 9(1), 1–9. <https://doi.org/10.1038/s41467-018-06254-6>

Piper, D. J. W., & Normark, W. R. (2009). Processes That Initiate Turbidity Currents and Their Influence on Turbidites: A Marine Geology Perspective. *Journal of Sedimentary Research*, 79(6), 347–362. <https://doi.org/10.2110/jsr.2009.046>

Piper, D. J. W., Cochonat, P., & Morrison, M. L. (1999). The sequence of events around the epicentre of the 1929 Grand Banks earthquake: initiation of debris flows and turbidity current inferred from sidescan sonar. *Sedimentology*, 46(1), 79–97.
<https://doi.org/10.1046/j.1365-3091.1999.00204.x>

Polonia, A., Vaiani, S. C., & De Lange, G. J. (2016). Did the A.D. 365 Crete earthquake/tsunami trigger synchronous giant turbidity currents in the Mediterranean Sea? *Geology*, 44(3), 191–194. <https://doi.org/10.1130/G37486.1>

Polonia, A., Nelson, C. H., Romano, S., Vaiani, S. C., Colizza, E., Gasparotto, G., & Gasperini, L. (2017). A depositional model for seismo-turbidites in confined basins based on Ionian Sea deposits. *Marine Geology*, 384, 177–198. <https://doi.org/10.1016/j.margeo.2016.05.010>

Pope, E. L., Talling, P. J., & Carter, L. (2017). Which earthquakes trigger damaging submarine mass movements: Insights from a global record of submarine cable breaks? *Marine Geology*, 384, 131–146. <https://doi.org/10.1016/j.margeo.2016.01.009>

Puig, P., Ogston, A. S., Mullenbach, B. L., Nittrouer, C. A., Parsons, J. D., & Sternberg, R. W. (2004). Storm-induced sediment gravity flows at the head of the Eel submarine canyon, northern California margin. *Journal of Geophysical Research: Oceans*, 109(C3), 1–10. <https://doi.org/10.1029/2003JC001918>

Şengör, A. M. C., Grall, C., İmren, C., Le Pichon, X., Görür, N., Henry, P., Karabulut, H., & Siyako, M. (2014). The geometry of the North Anatolian transform fault in the Sea of Marmara and its temporal evolution: implications for the development of intracontinental transform faults. *Canadian Journal of Earth Sciences*, 51(3), 222–242.
<https://doi.org/10.1139/cjes-2013-0160>

a supprimé: ¶

a supprimé: ¶

1400 Synolakis, C. E., Bardet, J.-P., Borrero, J. C., Davies, H. L., Okal, E. A., Silver, E. A., Sweet,
 1401 S., & Tappin, D. R. (2002). The slump origin of the 1998 Papua New Guinea Tsunami.
 1402 Proceedings of the Royal Society of London. Series A: Mathematical, Physical and
 1403 Engineering Sciences, 458(2020), 763–789. <https://doi.org/10.1098/rspa.2001.0915>
 1404 [Talling, P. J. \(2021\). Fidelity of turbidites as earthquake records. *Nature Geoscience*, 14\(3\),](#)
 1405 [113–116. <https://doi.org/10.1038/s41561-021-00707-2>](#)
 1406 [Talling, P. J., Masson, D. G., Sumner, E. J., & Malgesini, G. \(2012\). Subaqueous sediment](#)
 1407 [density flows: Depositional processes and deposit types. *Sedimentology*, 59\(7\), 1937–](#)
 1408 [2003. <https://doi.org/10.1111/j.1365-3091.2012.01353.x>](#)
 1409 Xu, J. P., Noble, M. A., & Rosenfeld, L. K. (2004). In-situ measurements of velocity structure
 1410 within turbidity currents. *Geophysical Research Letters*, 31(9).
 1411 <https://doi.org/10.1029/2004GL019718>
 1412 Xu, J. P., Swarzenski, P. W., Noble, M., & Li, A.-C. (2010). Event-driven sediment flux in
 1413 Hueneme and Mugu submarine canyons, southern California. *Marine Geology*, 269(1–
 1414 2), 74–88. <https://doi.org/10.1016/j.margeo.2009.12.007>
 1415 Yakupoğlu, N., Uçarkuş, G., Kadir Eriş, K., Henry, P., & Namık Çağatay, M. (2019).
 1416 Sedimentological and geochemical evidence for seismoturbidite generation in the
 1417 Kumburgaz Basin, Sea of Marmara: Implications for earthquake recurrence along the
 1418 Central High Segment of the North Anatolian Fault. *Sedimentary Geology*, 380, 31–44.
 1419 <https://doi.org/10.1016/j.sedgeo.2018.11.002>
 1420 Zitter, T. A. C., Grall, C., Henry, P., Özeren, M. S., Çağatay, M. N., Şengör, A. M. C.,
 1421 Gasperini, L., de Lépinay, B. M., & Géli, L. (2012). Distribution, morphology and triggers
 1422 of submarine mass wasting in the Sea of Marmara. *Marine Geology*, 329–331, 58–74.
 1423 <https://doi.org/10.1016/j.margeo.2012.09.002>

Page 26 : [1] a supprimé HENRY Pierre 19/09/2022 18:54:00

Page 26 : [2] a supprimé HENRY Pierre 19/09/2022 18:57:00

Page 26 : [3] a supprimé HENRY Pierre 19/09/2022 19:21:00

Page 26 : [4] a supprimé HENRY Pierre 19/09/2022 19:17:00